

PROPOSAL TO JEFFERSON LAB PAC 42
**Wide-angle Compton Scattering at
8 and 10 GeV Photon Energies**

D. J. Hamilton (co-spokesperson), J. R. M. Annand, D. I. Glazier, D. G. Ireland,
K. Livingston, I.J.D. MacGregor, B. McKinnon, B. Seitz, D. Sokhan
University of Glasgow, Glasgow, Scotland

S. Širca (co-spokesperson), J. Beričič, M. Mihovilovič, S. Štajner
J. Stefan Institute and Dept. of Physics, University of Ljubljana, Slovenia

B. Wojtsekhowski (spokesperson-contact), A. Camsonne, S. Covrig, P. Degtiarenko,
R. Ent, D. Gaskell, D. Higinbotham, M. K. Jones, C. Keppel, V. Kubarovksy,
D. Mack, P. Nadel-Turoński, B. Sawatzky, M. Ungaro, S. A. Wood
Thomas Jefferson National Accelerator Facility, Newport News, VA 23606

I. Albayrak, M. A. Pannunzio Carmignotto, J. Denes-Couto,
N. Hlavin, T. Horn, F. Klein, B. Nepal
The Catholic University of America, Washington, DC 20064

S. Abrahamyan, A. Asaturyan, A. Mkrtchyan, H. Mkrtchyan,
V. Tadevosyan, A. Shahinyan, H. Voskanyan, S. Zhamkochyan
A.I. Alikhanyan National Science Laboratory, Yerevan 0036, Armenia

V. Bellini, M. Capogni, E. Cisbani, A. Del Dotto, C. Fanelli, F. Garibaldi,
S. Frullani, F. Mammoliti, F. Noto, G. Salmé, M. C. Sutura, G. M. Urciuoli
INFN, Italy

G.B. Franklin, V. Mamyan, B. Quinn
Carnegie Mellon University, Pittsburgh, PA 15213

R. Gilman, K. Myers, R. Ransome
Rutgers, The State University of New Jersey, Piscataway, NJ 08854

D. Nikolenko, I. Rachek, Yu. Shestakov
Budker Institute, Novosibirsk, Russia

W. Boeglin, P. Markowitz
Florida International University, Miami, FL 33199

V. Punjabi
Norfolk State University, Norfolk, VA 23504

B. Vlahovic
North Carolina Central University, Durham, NC 03824

A. Ahmidouch, S. Danagoulian
North Carolina A&T State University, Greensboro, NC 27411

A. K. Opper, I. Strakovsky
The George Washington University, Washington, DC 20052

D. Androic
University of Zagreb, Zagreb, Croatia

M. Kohl
Hampton University, Hampton, VA 23668

T. Averett, C. Perdrisat
College of William and Mary, Williamsburg, VA 23185

J. Dunne, D. Dutta, M. H. Shabestari
Mississippi State University, Mississippi State, MS 39762

M. Amaryan, L. El Fassi, C. Hyde, A. Radyushkin, M. N. H. Rashad
Old Dominion University, Norfolk, VA 23529

D. Day, R. Lindgren, D. Keller, N. Liyanage, B. E. Norum, O. Rondon, J. Zhang
University of Virginia, Charlottesville, VA 22901

P. Solvignon
University of New Hampshire, Durham, NH 03824

F. Sabatié
CEA Saclay—Irfu/SPhN

C. Muñoz Camacho
Institut de Physique Nucleaire d'Orsay, IN2P3, BP 1, 91406 Orsay, France

Z. Ahmed, G. M. Huber, W. Li, D. Paudyal
University of Regina, Regina, SK S4S 0A2

and

The Neutral Particle Spectrometer collaboration:
<https://wiki.jlab.org/cuawiki/index.php/Collaboration>

May 31, 2014

Neutral Particle Spectrometer (NPS) Collaboration

A. Camsonne, R. Ent, P. Nadel-Turoński, S. A. Wood, B. Wojtsekhowski, C. Zorn
Jefferson Lab, Newport News, VA 23606

A. Asaturyan, A. Mkrtchyan, H. Mkrtchyan, V. Tadevosyan, S. Zhamkochyan
A.I. Alikhanyan National Science Laboratory, Yerevan 0036, Armenia

M. Guidal, C. Munoz Camacho, R. Paremuzyan
Institut de Physique Nucleaire d'Orsay, IN2P3, BP 1, 91406 Orsay, France

I. Albayrak, M. Carmignotto, N. Hlavin, T. Horn, F. Klein, B. Nepal, I. Sapkota
The Catholic University of America, Washington, DC 20064

C. Hyde, M. N. H. Rashad
Old Dominion University, Norfolk, VA 23529

P. King, J. Roche
Ohio University, Athens, OH 45701

D. Day, D. Keller, O. Rondon, J. Zhang
University of Virginia, Charlottesville, VA 22901

J. R. M. Annand, D. J. Hamilton
University of Glasgow, Glasgow, Scotland, UK

S. Širca
University of Ljubljana, Ljubljana, Slovenia

D. Dutta
Mississippi State University, Starkville, MS 39762

Contents

1	Introduction	6
2	Physics Motivation	9
2.1	Two-photon Physics in the SCET	9
2.2	Handbag Mechanism and GPD-based Models	10
2.3	Real Compton Scattering in the DSE approach	12
2.4	Relativistic Constituent Quark Model	14
2.5	pQCD Mechanism	14
2.6	Summary of Physics Goals and Selection of Kinematics	15
2.7	Neutral Pion Photoproduction	21
3	Experimental Setup	22
3.1	The CEBAF Electron Beam	23
3.2	The Liquid Hydrogen Target and Radiator	23
3.3	The High-Momentum Spectrometer	23
3.4	Deflection Magnet	24
3.5	The Photon Calorimeter	26
3.6	Trigger, DAQ and Computing Requirements	28
3.7	Radiation Effects	28
4	Proposed Measurements	31
4.1	Kinematic Settings	31
4.2	Monte Carlo Simulation	32
4.3	Expected Event Rate and Statistical Precision	35
4.4	Systematic Uncertainties	37
5	Beam-Time Request and Expected Results	41
6	Conclusion	44

Abstract

We propose an experiment to measure the cross-section for Real Compton Scattering (RCS) from the proton in Hall C at incident photon energies of 8 GeV ($s = 15.9 \text{ GeV}^2$) and 10 GeV ($s = 19.6 \text{ GeV}^2$) over a broad span of scattering angles in the wide-angle regime. With 425 hours (18 days) of beam-time, high precision data in a previously unexplored kinematic regime will be obtained.

The experiment will utilize an untagged bremsstrahlung photon beam and the standard cryogenic liquid hydrogen target. The scattered photon will be detected in the new NPS photon spectrometer, presently under construction in Hall C. The electron beam will pass through the target, while the electrons scattered in the direction of the calorimeter will be deflected by a small magnet which will allow for discrimination between the Compton and elastic electron scattering processes. The recoil protons will be detected in the Hall C HMS magnetic spectrometer.

In the proposed experiment we will perform precise cross-section measurements at the highest possible photon energies over a broad kinematic range. These results will be essential in order to confirm whether the factorization regime has been attained and investigate the nature of the factorized reaction mechanism. Understanding this simplest of processes, which involves only two real photons and a single hadron, will provide a solid foundation for the understanding of other photo-induced exclusive reactions in the JLab energy range. Moreover, the universality of the underlying nucleon form-factors means that these data will be extremely valuable in understanding high momentum transfer data for two-photon exchange effects in elastic electron-nucleon scattering, time-like Compton scattering and other hard exclusive reactions.

We have taken into account the PAC 40 recommendation to try to refocus the experiment in terms of the kinematic range, and to offer a very detailed explanation of how the proposed measurements will help lead to systematic improvements in the various theories of WACS. This is handled in Sec. 2.6, comprising one of the two major changes in the text since the first proposal. The other is a complete rewrite of the sections dealing with the simulation (Sec. 4.2) and in particular the sections describing the way data is actually going to be analyzed (Secs. 4.3 and 4.4).

1 Introduction

Compton scattering in the hard scattering limit is a powerful probe of the structure of the nucleon. In the wide-angle regime (WACS) it provides access to the high- t transverse structure of the hadron, whilst in the deeply-virtual (DVCS) regime it provides access to its high- Q^2 , low- t structure. WACS is therefore a natural complement to other exclusive reactions such as high- Q^2 elastic electron scattering and high-energy meson photo-production. Two-photon coupling to the hadron allows access to non-perturbative structure information which is not available from DIS approaches and is important in elastic electron scattering. At the same time, data on the WACS process is likely to be more suitable for theoretical analysis than on other more complex photo-induced reactions. A substantial previous body of theoretical predictions exists based on the GPD-based handbag approach [1, 2, 3], the relativistic constituent quark model [4] and the perturbative QCD (pQCD) mechanism [5, 6]. Largely motivated by the potential offered by the JLab upgrade, the last few years have seen three exciting new theoretical advances which seek to further our understanding of this fundamental reaction.

The first of these is based upon new calculations by N. Kivel and M. Vanderhaeghen [7, 8] of two-photon effects in the *Soft-Collinear Effective Theory* (SCET). This work has established the factorization of the handbag mechanism into hard and soft-collinear contributions. The SCET approach has also provided a phenomenological analysis of the WACS observables and introduced a new universal nucleon form factor, the magnitude of which has been extracted from previous JLab data. The second recent advance is also based upon the handbag mechanism and has involved updating the *GPD-based analysis* of electron-nucleon scattering form factors and WACS by M. Diehl and P. Kroll [9]. This has led to a refined prediction of the high-energy WACS cross-section and the GPD-based form factors on which it is based. Thirdly, a formalism for the RCS process based on the *Dyson-Schwinger Equation* (DSE) approach has been proposed by G. Eichmann and C. Fisher [10]. The specific results for the WACS observables in this framework have not yet been published, but the advances in the elastic form-factor calculations that have been achieved [11, 26] augur well for a promising microscopic theory of WACS in the near future.

For real-photon Compton scattering, the hard scale is achieved when s , $-t$, and $-u$ are all large compared with the proton mass or, equivalently, when the transverse momentum transfer p_\perp is large (the WACS regime). Under such conditions one expects the transition amplitude to factorize into the convolution of a perturbative hard scattering amplitude, which involves the coupling of the external photons to the active quarks, with an overlap of initial and final soft (non-perturbative) wave-functions, which describes the coupling of the active quarks to the proton. Schematically this can be written as

$$T_{if}(s, t) = \Psi_f \otimes K(s, t) \otimes \Psi_i, \quad (1)$$

where $K(s, t)$ is the perturbative hard scattering amplitude, and the Ψ 's are soft wave-functions. Different factorization schemes have been applied to RCS in recent years and these can be distinguished by the number of active constituents participating in the hard scattering sub-process. The handbag mechanism [1, 2, 3, 9] involves only one active constituent, while the pQCD mechanism [5, 12, 6, 13, 14] involves three. In any given kinematic regime, both

mechanisms will contribute — in principle — to the scattering amplitude. At “sufficiently high” energy the pQCD mechanism is expected to dominate, but it is neither known how high is “sufficiently high” nor in what manner the transition to the purely pQCD mechanism occurs.

At relatively low energies (e.g. in the resonance region), RCS and other exclusive reactions are dominated by purely soft physics, and the amplitude does not factorize into hard and soft processes. At high energies but small $-t$ or $-u$, soft physics also dominates through Regge exchanges [15]. The nature of the transition from purely soft to the factorization regime is not well known. Quite aside from the reaction mechanism, it is of interest to ask what RCS can teach us about the non-perturbative structure of the proton and to relate it to that revealed in other reactions.

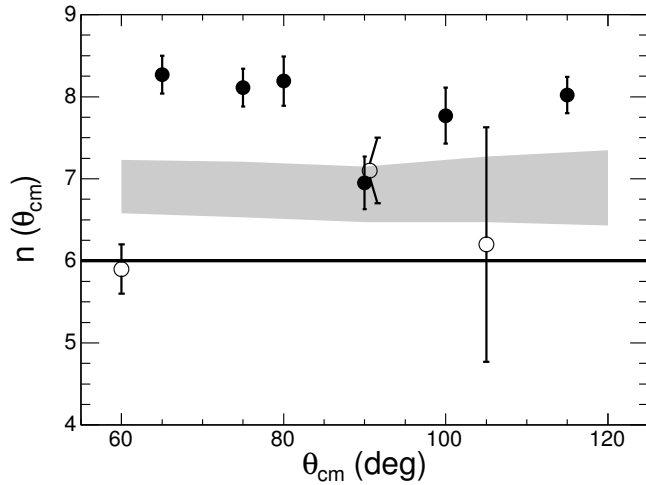


Figure 1: Scaling of the RCS cross-section at fixed θ_{cm} . Full symbols denote the data from the E99-114 experiment [16]. The solid line corresponds to a constituent counting rule and scaling with a fixed value $n = 6$. Open symbols denote the data from the Cornell experiment [17]. The gray band shows the range allowed by the GPD-based calculations of [3].

With this backdrop, JLab Hall A experiment E99-114 [18] was undertaken to study the RCS reaction. The primary focus was the measurement of precise spin-averaged cross-sections over the kinematic regime of $5 \leq s \leq 11 \text{ GeV}^2$ and $1.5 \leq -t \leq 6.5 \text{ GeV}^2$. The measurement produced the important result that the scaling of the cross-section is in unambiguous disagreement with the pQCD prediction [16], as shown in Fig. 1. In addition, a measurement was made at a single kinematic point of the polarization transfer to the recoil proton by using circularly polarized incident photons. The latter measurement has produced the result [19] shown in Fig. 2 that the longitudinal polarization transfer is consistent with the handbag predictions, while it is completely inconsistent with predictions based on pQCD. This gives very strong credence to the notion that — at least in this energy range — the photons interact with a single quark. Indeed, the longitudinal polarization is nearly as large as that expected for scattering from a free quark. Because there was only one such polarization measurement made during E99-114, a similar experiment (E07-002) at higher s was undertaken in Hall C, the analysis of which is at an advanced stage [20].

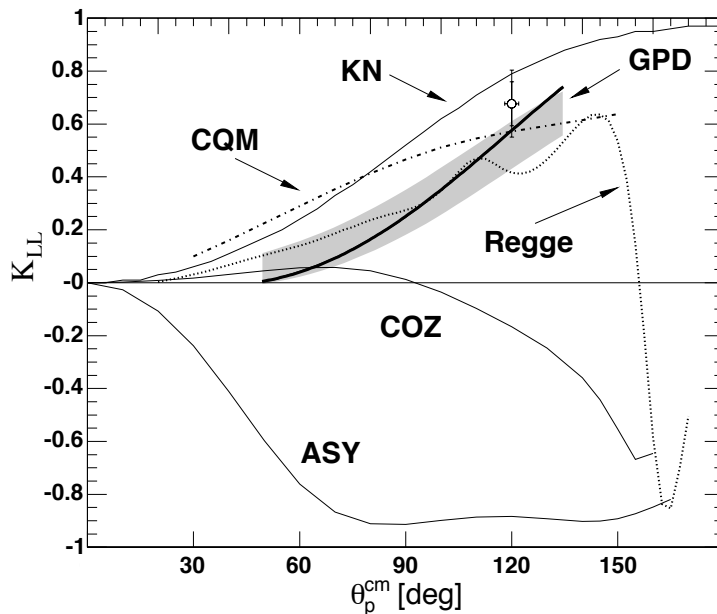


Figure 2: Longitudinal polarization transfer coefficient in the RCS process at an incident energy of 3.23 GeV [19]. The labels are: KN for the asymmetry in the hard subprocess; GPD (shown as a gray band) for the handbag approach using GPDs [21]; CQM for the handbag approach by using constituent quarks [4]; Regge for a Regge-exchange mechanism [22]; and COZ and ASY for pQCD calculations [13] by using the asymptotic (ASY) or Chernyak-Ogloblin-Zhitnitsky (COZ) distribution amplitudes.

These results are so intriguing that it is essential to verify E99-114 findings with measurements over a broader kinematic range, especially for higher photon energies. We propose new measurements of the differential cross-section in Compton scattering at incident energies of 8 and 10 GeV, or $s = 15.9$ and 19.6 GeV^2 , respectively, over a broad span of scattering angles ranging from $\theta_{\text{cm}} = 49^\circ$ to 105° . These will constitute the first measurements ever to investigate WACS at photon energies above 6 GeV. The range of the variable $-t$ will be approximately doubled compared with the previous experiment [18]. As the values of s , $-t$ and $-u$ will all be much larger than the proton mass, and the data therefore unambiguously in the wide-angle regime, the experiment will provide a much firmer grip on the manner in which factorization is realized. Even if a definitive answer to this question remains elusive, the experiment will provide unique data for testing QCD-based theories and will serve as an important input for two-photon exchange calculations and nucleon structure models that are relevant to a wide variety of reactions.

The proposal is organized as follows: in Sec. 2 we present our physics motivation and summarize the physics goals of the proposed experiment. The experimental approach including a description of both the standard and specialized equipment that will be used is described in Sec. 3. In the subsequent sections, we then present our proposed measurements (Sec. 4) and our expected results and beam-time request (Sec. 5).

2 Physics Motivation

In view of the remarks made in the previous section, we consider several crucial questions of a general nature that motivate the further exploration of the WACS cross section at JLab:

1. Is it indeed true that the reaction proceeds through the interaction of the photons with a single quark?
2. What information can be obtained about the non-perturbative structure of the proton, and how can it be related to that obtained from experiments on other hard exclusive reactions?
3. At what energy scale does the transition from soft to hard factorization mechanisms occur?

In the following subsections we briefly present a discussion of WACS in the soft-collinear effective theory, the handbag approach with GPDs, the still embryonic DSE development, the relativistic constituent quark model and the pQCD mechanism. Finally, the motivation for the choice of kinematics settings in the current proposal is presented, with a view to focus on the specific questions given above while maintaining as modest a beam-time request as is practical.

2.1 Two-photon Physics in the SCET

The soft-collinear effective theory (SCET) was recently developed for elastic electron-proton scattering at high momentum transfer [7]. The QCD factorization approach formulated in the framework of SCET allows one to develop a description of the soft-spectator scattering contribution to the overall amplitude. The two-photon exchange (TPE) corrections to elastic electron-proton scattering were calculated in the region where the kinematic variables are moderately large relative to the soft hadronic scales (M_p and Λ_{QCD}). This calculation factorizes the TPE contributions by introducing a single, universal SCET form-factor $\mathcal{F}_1(Q)$ that defines the dominant underlying amplitudes. As the same form factor also naturally arises in wide-angle Compton scattering, the authors of Refs. [7, 8] argue that the most promising route for understanding the soft spectator contribution in hard exclusive reactions at JLab energies is through the study of WACS.

The unpolarized cross-section describing Compton scattering in the SCET approach has the form:

$$\frac{d\sigma}{dt} \simeq \frac{2\pi\alpha^2}{(s-m^2)^2} \left(\frac{1}{1-t/s} + 1 - t/s \right) |\mathcal{R}|^2 = \frac{d\sigma^{\text{KN}}}{dt} |\mathcal{R}|^2, \quad (2)$$

where $d\sigma^{\text{KN}}$ is the Klein-Nishina cross-section corresponding to a point-like massless particle. The values $|\mathcal{R}| = \sqrt{d\sigma^{\text{exp}}(s, t)/d\sigma^{\text{KN}}(s, t)}$ extracted from the E99-114 data [16] are shown in Fig. 3 taken from Ref. [8] as a function of $-t$ and s . This plot shows calculations at three different values of beam energy, corresponding to $s = 6.8, 8.9$ and 10.9 GeV^2 at $2.5 < -t < 6.5 \text{ GeV}^2$. As one can see from this plot, the extracted values of the SCET form-factor do not show any significant dependence on the values of s , as required by factorization.

However, at the highest values of t data is only available for a single value of s . The primary motivation for the current proposal is therefore to extend the kinematic range over which $|\mathcal{R}|$ can be extracted in order to explore further its s -independence, and to provide valuable input for high momentum transfer data on both elastic and time-like form-factors.

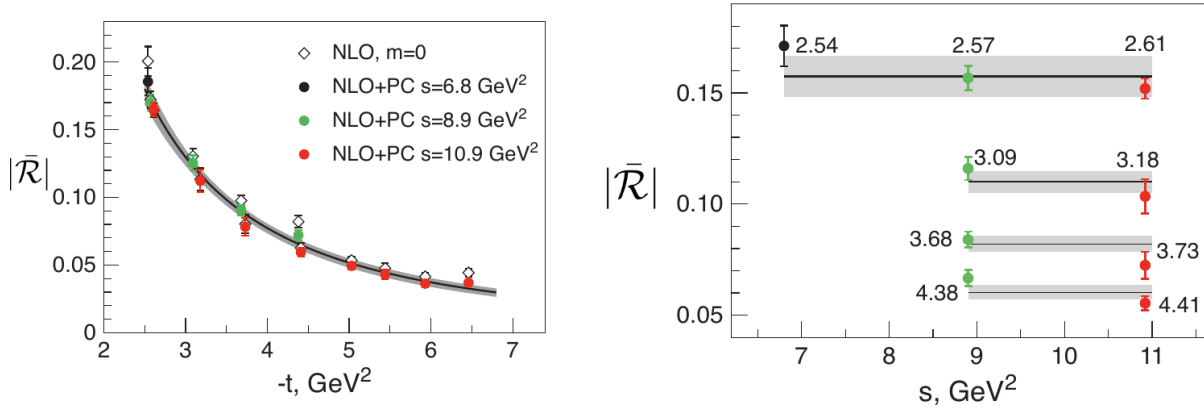


Figure 3: The ratio \mathcal{R} extracted from the E99-114 data [16] as a function of $-t$ (left) and s (right) [7, 8]. The gray band shows the 1σ error bands of the kinematic power-corrected fit to the form-factor.

2.2 Handbag Mechanism and GPD-based Models

The handbag mechanism within a GPD-based framework has in recent years become a staple in the interpretation of hard exclusive reactions. It has provided a self-consistent framework for the interpretation of so-called deep exclusive reactions, which are reactions initiated by a high- Q^2 virtual photon. The application of this formalism to RCS (see Fig. 4) was initially worked out to leading order (LO) by A. Radyushkin [1], by M. Diehl and collaborators [2], and at next-to-leading-order (NLO) by H. Huang and P. Kroll [3]. A very recent new analysis for WACS at JLab upgrade energies has been performed by Diehl and Kroll [9]

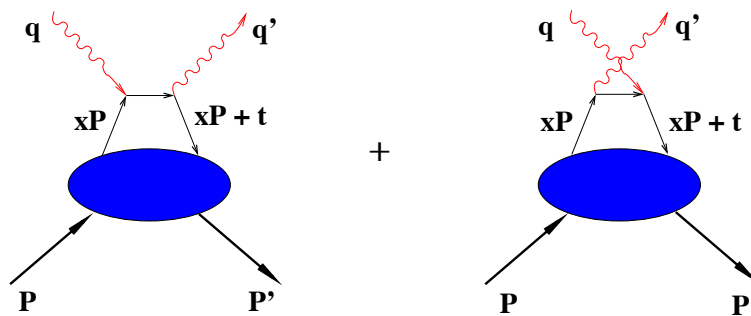


Figure 4: The handbag diagram (left) and the crossed term (right) for RCS.

The handbag approach shares many of the features present in the SCET approach: the hard-scale physics is contained in the scattering from a single active quark and is calculable using pQCD and QED as it is simply Compton scattering from a structureless spin-1/2 particle. The soft physics is contained in the wave-functions describing how the active quark

couples to the proton. This coupling, and the underlying wave-functions, is fully described in terms of GPDs.

GPDs have been the subject of intense experimental and theoretical activity in recent years since the original articles first appeared [23, 24]. They represent “superstructures” of the nucleon, from which other measurable structure functions are derived, such as parton distribution functions (PDF) and form-factors. To NLO, only three of the four GPDs contribute to the WACS process: $H(x, \xi = 0, t)$, $\hat{H}(x, \xi = 0, t)$, and $E(x, \xi = 0, t)$. Since the photons are both real, the so-called skewness parameter $\xi = 0$, reflecting the fact that the momentum absorbed by the struck quark is purely transverse.

In the handbag formalism, the RCS observables are new form-factors of the proton that are x^{-1} -moments of the GPDs:

$$\begin{aligned} R_V(t) &= \sum_a e_a^2 \int_{-1}^1 \frac{dx}{x} H^a(x, 0, t), \\ R_A(t) &= \sum_a e_a^2 \int_{-1}^1 \frac{dx}{x} \text{sign}(x) \hat{H}^a(x, 0, t), \\ R_T(t) &= \sum_a e_a^2 \int_{-1}^1 \frac{dx}{x} E^a(x, 0, t), \end{aligned}$$

where e_a is the charge of the active quark and the three form factors are, respectively, the vector, axial vector, and tensor form-factors. The corresponding form-factors for elastic electron or neutrino scattering are given by the x^0 -moments of the same GPDs:

$$\begin{aligned} F_1(t) &= \sum_a e_a \int_{-1}^1 dx H^a(x, 0, t), \\ G_A(t) &= \sum_a \int_{-1}^1 dx \text{sign}(x) \hat{H}^a(x, 0, t), \\ F_2(t) &= \sum_a e_a \int_{-1}^1 dx E^a(x, 0, t), \end{aligned}$$

where the three quantities are, respectively, the Dirac, axial, and Pauli form-factors. On the other hand, the $t = 0$ limit of the GPDs produce the PDFs:

$$\begin{aligned} H^a(x, 0, 0) &= q^a(x), \\ \hat{H}^a(x, 0, 0) &= \Delta q^a(x), \\ E^a(x, 0, 0) &= 2 \frac{J^a(x)}{x} - q^a(x), \end{aligned} \tag{3}$$

where J^a is the total angular momentum of quark flavor a and is not directly measurable in DIS.

Equations for the form-factors based on the underlying helicity amplitudes for WACS lead to expressions relating experimental observables to these form-factors. The most important of these is the spin-averaged cross-section, which factorizes into a simple product of the

Klein-Nishina (KN) cross-section describing the hard scattering from a single quark and a sum of form-factors depending only on t [1, 2]:

$$\frac{d\sigma/dt}{d\sigma_{\text{KN}}/dt} = f_V \left[R_V^2(t) + \frac{-t}{4m^2} R_T^2(t) \right] + (1 - f_V) R_A^2(t). \quad (4)$$

For the interesting region of large p_\perp , the kinematic factor f_V is always close to 1. Consequently the unpolarized cross sections are largely insensitive to R_A , and the left-hand-side of Eq. (4) is nearly s -independent at fixed t . The NLO calculations, which take into account both photon and proton helicity-flip amplitudes, do not change this prediction in any appreciable way [3]. A new analysis of the GPDs recently performed by Diehl and Kroll [9] gave an updated prediction for the WACS cross-section, as can be seen in Fig. 5.

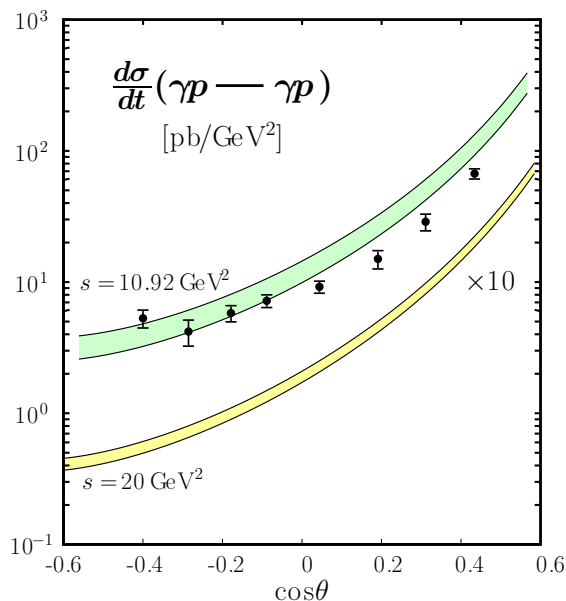


Figure 5: The most recent GPD-based prediction for the WACS cross section at $s = 10.92 \text{ GeV}^2$ and $s = 20 \text{ GeV}^2$ from Diehl and Kroll [9].

2.3 Real Compton Scattering in the DSE approach

For all the insight that we gain from pQCD, we learn rather little about many of the most important issues concerning nucleon structure, such as the dynamical generation of mass through Dynamical Chiral Symmetry Breaking (DCSB), or quark confinement. There are, however, analytical techniques that at least in principle appear to have the potential to provide solutions to QCD in the non-perturbative regime with arbitrarily high accuracy. One such technique is based on the infinite tower of Dyson-Schwinger equations (DSEs) that relate the Green's functions of a field theory to each other [25]. In principle, solving the DSEs provides a solution to any field theory. In any practical calculation, however, the DSEs must be truncated, and some Ansätze must be employed to account for the omitted

functions. By carefully maintaining certain properties of the theory, however, such as local and global symmetries, considerable progress can be made. Recent calculations, for instance, explicitly describe the dynamic generation of the mass of constituent quarks, and show excellent agreement with the lattice QCD results that necessarily assume large current-quark masses. In Fig. 6 the dressed-quark mass function $M(p)$ is shown as a function of momentum for each of three bare-quark masses.

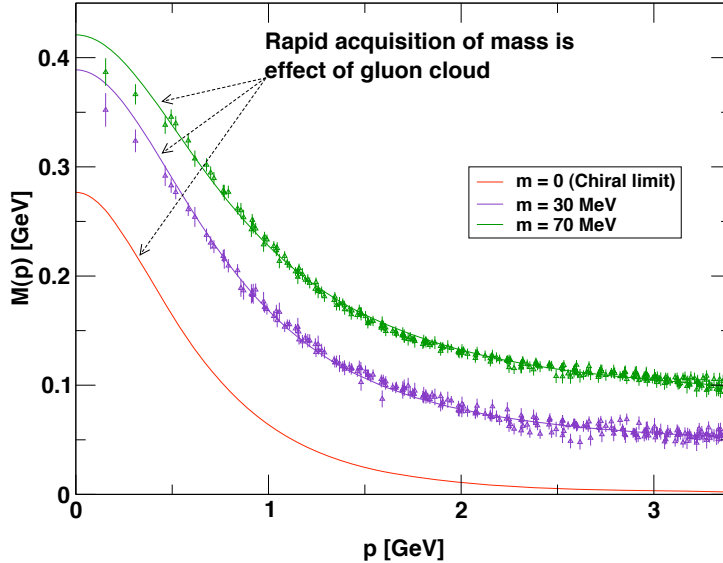


Figure 6: Dressed-quark mass function, $M(p)$. The solid curves show DSE results and the “data” represent unquenched LQCD calculations. In this figure one observes the current-quark of perturbative QCD evolving into a constituent-quark as its momentum becomes smaller.

Using dressed quarks as the elementary degrees of freedom, one can calculate nucleon form-factors using a Poincaré-covariant Faddeev equation, as has been done recently by C. D. Roberts and collaborators [11, 26]. These authors also assume that two of the quarks couple into a diquark. While still an approximation, the DSE/Faddeev approach is in part based on first principles. It is limited, however, in that there are precisely three (and for instance, not five) constituent quarks used as an input to the calculation. Even so, it is reasonable to assume the dominance of the three-quark component of the wave-function at relatively high values of Q^2 . The DSE/Faddeev calculations provide a remarkably good description of the available elastic electron-nucleon form-factor data, which is likely telling us a fairly profound fact about the nucleon’s structure.

These advances in the form-factors calculations have led to the expectation that the WACS process could also be calculated in the DSE approach. Indeed, in a recent paper [10] the relevant phenomenology for the RCS reaction has been developed. However, the calculations for specific observables are not yet available. Work towards this goal is progressing through calculations on the light-by-light contribution to the muon’s anomalous magnetic moment, $(g - 2)_\mu$, which relies on the same underlying building blocks, and low- t space-like Compton scattering [27].

2.4 Relativistic Constituent Quark Model

A formulation for RCS in the handbag approach that differs significantly from the GPD formalism, but shares some of the conceptual features of the DSE framework, is that of Miller [4]. In his approach the handbag diagram involves γq scattering, as before, and proton wave-functions obtained from relativistic Constituent Quark Models (CQM). What distinguishes this approach from the SCET, GPD and pQCD models is the fact that these proton wave-functions explicitly include the influence of quark transverse momenta and configurations involving non-zero quark orbital angular momentum. This naturally corresponds to violation of proton helicity conservation. Indeed, non-conservation of proton helicity in this model has proven to be one of the key factors in its successful account of electromagnetic form-factor data for the proton [28, 29].

The calculations for RCS involve evaluating the handbag diagrams of Fig. 4 in impulse approximation. The resulting reaction amplitude depends on proton wave-functions obtained from Poincaré-invariant calculations involving constituent quark models in light-front dynamics. These wave-functions have previously been constrained by proton electromagnetic form-factor data in the same kinematic regime [29]. Significant contributions to the wave functions from quark transverse momenta and orbital angular momentum are a natural feature of the relativistic calculations. Reasonable agreement with RCS cross-section data has been obtained with a slight modification of the constituent quark masses [4].

2.5 pQCD Mechanism

Historically, the traditional framework for the interpretation of hard exclusive reactions has been perturbative QCD (pQCD) [30]. This is based in part on the observation that the onset of scaling in Deep Inelastic Scattering (DIS) occurs at the relatively low scale of $Q^2 \approx 1\text{--}2 \text{ (GeV/c)}^2$, thereby giving rise to expectations that pQCD might also be applicable to exclusive processes in the range of a few GeV^2 . The pQCD approach to RCS [5, 12, 6, 13, 14] is shown in Fig. 3, where it is seen that all three valence quarks are active participants in the hard subprocess, which is effected by the exchange of two hard gluons, while the soft physics is contained in the valence quark distribution amplitudes.

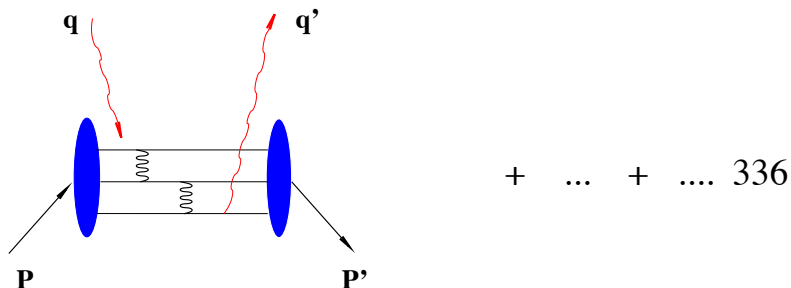


Figure 7: Two-gluon exchange pQCD diagram for WACCS.

The pQCD mechanism leads naturally to the so-called constituent counting rules for

exclusive processes:

$$\frac{d\sigma}{dt} = \frac{f(\theta_{\text{cm}})}{s^n}, \quad (5)$$

where n is related to the number of active constituents in the reaction [31, 32]. Indeed, the observation that many exclusive reactions, such as elastic electron scattering, pion photo-production, and RCS, approximately obey Eq. (5), has led to the belief that the pQCD mechanism dominates at experimentally accessible energies. There seems to be little theoretical disagreement that the pQCD mechanism dominates at sufficiently high energies [33]; however, there is no consensus on how high is “sufficiently high”.

A recalculation of the pQCD mechanism and reassessment in light of the E99-114 data has been completed by Thompson et al. [14]. The authors argue that the observed decrease in the scaled cross section as s increases is consistent with a view that the onset of the asymptotic regime will soon be accessible. Moreover, some commonality between the pQCD and handbag mechanisms has been indicated, with the suggestion that inclusion of higher twist effects will introduce the necessary proton helicity-flip contributions in order to better account for available data. However, calculations in the same reference demonstrate that in order to achieve agreement with the available JLab data the exchange gluon momentum transfer needs to be $Q^2 \gtrsim 0.02 s$, where s is the usual Mandelstam invariant. This value is very far from the hard QCD scale, and it is quite a stretch to believe that the asymptotic scale will be reached by the proposed doubling the range of s and $-t$.

2.6 Summary of Physics Goals and Selection of Kinematics

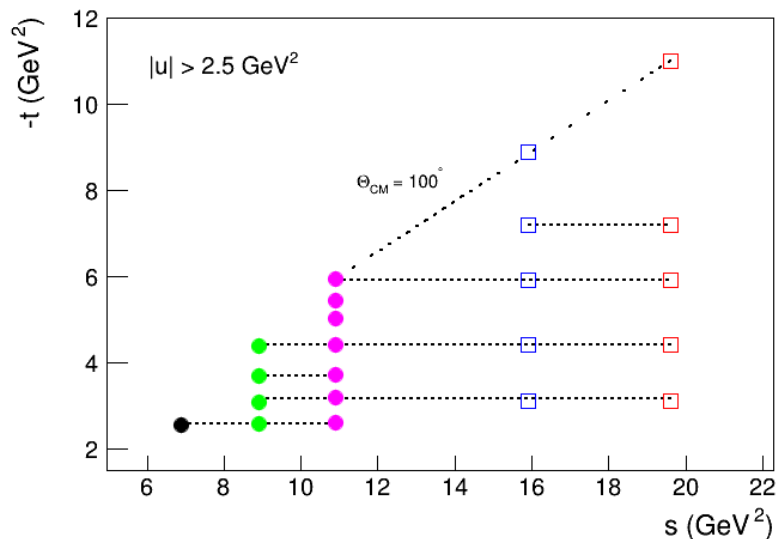


Figure 8: Kinematic settings as a function of s and $-t$ for the previous JLab E99-114 experiment (black, green and magenta) and the current proposal (blue and red open squares).

PAC 40 felt that with regards to the proposal that was submitted last year (PR12-13-009) it might be more promising to focus the experiment on a more restricted range of t , and

rather extend the s -range of the previous E99-114 experiment. We are therefore proposing a significantly reduced beam-time request based on a much more focused set of goals, while maintaining much of the original proposal’s richness in scope and horizon. While reduced compared to last year’s request, the extension in kinematic coverage offered in the new proposal is still ambitious. This can clearly be seen in Fig. 8, which shows the proposed kinematic settings as a function of s and $-t$ compared to the E99-114 data-set (only the points for which $-u > 2 \text{ GeV}^2$ are shown). A summary of the proposed kinematic settings are given in Table 1.

Table 1: Kinematics variables for WACS in five settings with a 4-pass, 8.8 GeV electron beam (4A–4E) and five settings with a 5-pass, 11 GeV electron beam (5A–5E).

Kin	θ^{cm} [$^\circ$]	s [GeV^2]	$-t$ [GeV^2]	$-u$ [GeV^2]
4A	55.8	15.89	3.10	11.03
4B	67.6	15.89	4.39	9.75
4C	80.4	15.89	5.91	8.22
4D	90.9	15.89	7.20	6.93
4E	104.8	15.89	8.90	5.23
5A	48.9	19.65	3.07	14.81
5B	59.5	19.65	4.41	13.47
5C	70.1	19.65	5.91	11.97
5D	78.7	19.65	7.21	10.68
5E	103.2	19.65	11.01	6.88

As can be seen in the figure and table, the main focus of the current proposal are four fixed $-t$ scans (4A–4D and 5A–5D), chosen such that three of them will overlap with the previous JLab data. These are intended to serve as a rigorous test of factorization in the WACS reaction over the fullest possible kinematic range. Indeed, the reasonably broad range in $-t$ will allow a test of the s -independence of the Compton form-factor \mathcal{R} and thereby firmly establish the validity of factorization. Having done so, we propose a high $-t$ point for each of the two beam energies (4E and 5E) in order to further extend the kinematic range and allow us to address the more specific questions discussed below.

Building on the general questions that are given at the start of this section, the specific physics goals motivating the current proposal are:

1. To measure precisely the WACS cross-sections at photon energies of 8 and 10 GeV, which is significantly above the kinematic range of any previous experiment. The overall statistical precision of the measurements will be discussed in Sec. 5.
2. (SCET) To test the universality of the form-factor \mathcal{R} and its relevance to other hard exclusive reactions. In doing so, the two-photon exchange (TPE) contribution to the

elastic form factors will be constrained in a new kinematic regime that will be measured by other 12 GeV experiments at JLab. In addition, one will be able to compare the role of time-like and space-like processes in Compton and elastic scattering.

3. (GPD) Much of what applies to the soft spectator contribution in SCET in terms of factorization can also be directly applied to the GPD-based handbag approach. Moreover, extraction of the Compton form-factors from the new data will allow for a phenomenological comparison with the elastic form-factors, which differ in the relation to the underlying GPDs by their relative momentum fraction (x) weightings.
4. (DSE) The proposed points at moderate $-t$ will help with future improvements in the DSE Compton scattering approach in terms of constraining the extrapolations from near the t -channel poles, where the dominant structure is assumed to reside.

Expanding on these points, the following discussion includes a more detailed explanation of how the proposed measurements will help lead to systematic improvements in the various models for WACS.

SCET: Testing the s - and t -dependence of \mathcal{R}

The new data will allow for a test of the s -dependence of the form factor \mathcal{R} , which can be directly predicted from theory. The kinematic points 4A–4C and 5A–5C will allow for verification of the s -dependence over a wide range of 6.8 – 19.6 GeV^2 . Although there is no previous data with which to compare, the s -dependence will also be tested in an entirely new kinematic regime by the proposed measurements at points 4D and 5D. This is a substantial systematic improvement of the validity of the SCET model because at present time only data at $s = 6.8$ and 8.9 GeV^2 for the same fixed values of $-t$ are available, as shown in Fig. 9.

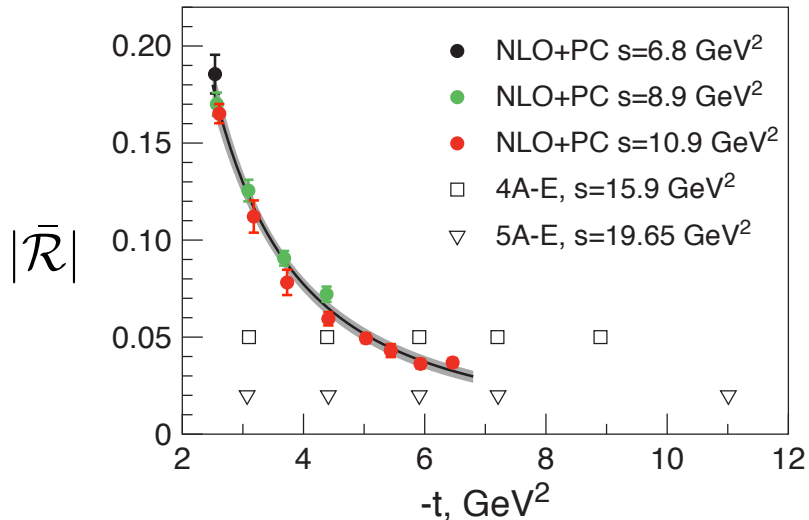


Figure 9: Extracted values of the SCET WACS form-factor \mathcal{R} for E99-114 data (black, green and red points). The kinematic points proposed in the current document are shown as open squares for $s = 15.9 \text{ GeV}^2$ and triangles for $s = 19.6 \text{ GeV}^2$.

It is not possible within the SCET approach to directly provide a prediction for the t -dependence of \mathcal{R} . Instead, if the s -dependence is in agreement with the theoretical expectations, then one can fit the data in order to extract the function $\mathcal{R}(t)$ as has been done in Fig. 9. As one moves to higher momentum transfer, the interplay between the competing sub-processes will evolve, meaning that it could be the case that the empirical fit used before will no longer describe the new data. If this were true, a more suitable ansatz that applies in this new kinematic regime would need to be found.

In either case, the new data will allow for the extraction of the t -dependence of the form-factor up to $-t = 11 \text{ GeV}^2$ (5E). The obtained values for $\mathcal{R}(t)$, coupled with its universal nature means that it can be used to account for the highly topical and important two-photon exchange (TPE) ambiguity in elastic ep-scattering, where the corresponding cross-sections will be measured up to $Q^2 = 17 (\text{GeV}/c)^2$. This will not possible with the other hadronic models for TPE at such high momentum transfer.

SCET: Soft-overlap contribution in other reactions

In the SCET framework the amplitude \mathcal{R} is associated with the soft overlap contribution which at some asymptotic values of s and $-t$ must be much smaller than the hard-spectator contribution which has been neglected in the present calculations. Therefore the proposed WACS data can clarify the energy range where the assumption about the dominance of the soft-overlap contribution is valid.

Within the SCET (or factorization) approach a similar reasoning applies also to the large- Q^2 behavior of the nucleon electromagnetic form-factors. Therefore WACS data are also useful for the theoretical interpretation of their large- Q^2 behavior. This becomes especially interesting if one considers the time-like (tl) and space-like (sl) kinematics. The WACS data above $-t = 8 \text{ GeV}^2$ will allow the theorists to compare R_{sl} and R_{tl} , the latter of which can be extracted from the $\gamma + \gamma \leftrightarrow p + \bar{p}$ reaction at large angles.

Kivel and Vanderhaeghen [34] have already carried out such analyses for existing time-like data from BELLE, and have observed that the time-like soft amplitude is double its space-like counterpart. However, to make the comparison more robust and better match the space-like and time-like kinematic coverage, one would need to obtain R_{sl} at $-t \geq 8 \text{ GeV}^2$. Hence, using the new WACS data from JLab (4E and 5E) one would be able to perform an explicit comparison of the time-like and space-like amplitudes \mathcal{R} . A similar analysis has been done on the elastic form-factors, which has found that at $Q^2 = 7 (\text{GeV}/c)^2$, $F_{\text{sl}}/F_{\text{tl}} \simeq 0.42$. Such an enhancement in the time-like region provides a strong indication that the dominance of the soft-overlap contribution is even more pronounced in these hadronic reactions, and leads to important questions as to why this should be the case.

GPD approach: Testing factorization

For testing factorization it is important to have a large lever arm in s at fixed $-t$, since the t -dependence itself is in part of non-perturbative origin. However, the present GPD-based theories cannot predict how well factorization works at given s and t , so it would not be wise to focus a program on a single value of $-t$. In addition, factorization in the wide-angle regime

requires not only large s and $-t$, but also large $-u$, which implies that at given s factorization will become worse beyond a certain $-t$ value. The range of $-t$ where factorization works is expected to increase with s , and quantitative exploration of this requires measurements over a sufficient $-t$ range. This point is illustrated — within the handbag approach and a specific model for the Compton form-factors as given in [9] — in Fig. 10.

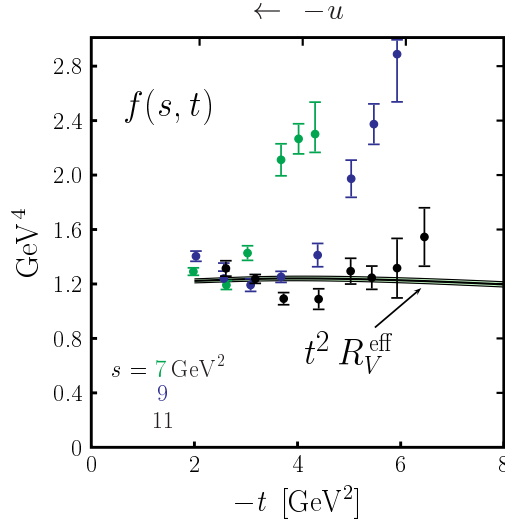


Figure 10: The range of $-t$ where the factorization of the Compton scattering amplitude works is expected to increase with s : with increasing s (green for $s = 7$, blue for $s = 9$ and black for $s = 11$ GeV^2 , respectively), the data line up increasingly well with the predicted flat dependence of $t^2 R_V^{\text{eff}}(t)$.

In kinematics where the handbag factorization holds, measuring the t -dependence allows one to extract the Compton form-factors; over a wide kinematic range this is essentially dominated by the form-factor $R_V(t)$, or a slight modification of it, $R_V^{\text{eff}}(t)$. This is a genuinely non-perturbative quantity that cannot be predicted in terms of other form-factors. However, its comparison with the nucleon Dirac form-factor F_1 — weighted with the appropriate square charges as $e_u^2 F_1^u(t) + e_d^2 F_1^d(t)$ — is indeed instructive, since within the handbag model the difference between the two quantities provides information on the momentum fractions x that dominate the form-factors when they are expressed as integrals over the GPDs. In particular, it is generically expected that the difference between Compton form-factor and its electro-magnetic counterpart should decrease with increasing $-t$. Quantitative exploration of this requires again measurements over an extended range in $-t$.

Dyson-Schwinger approach: Investigating the t -channel structure

The potentially promising Dyson-Schwinger Equation (DSE) approach to Compton scattering is still under development [10, 27], but the first results in this direction are expected within a year. The authors are presently testing the framework in a simpler system — the hadronic light-by-light contribution to $(g-2)_\mu$ — as it depends on the same underlying building blocks (the quark Compton vertex) and satisfies gauge invariance automatically — in contrast to Compton scattering, where (at least in the first stage) one is restricted to the

handbag/ t -channel contribution plus the nucleon resonance terms. The next steps towards the full treatment of Compton scattering will be in the space-like region: nucleon forward polarizabilities, two-photon corrections to form-factors, and possibly the proton radius puzzle. In this context, one can compare our proposed data points with the phase space that are accessible in the DSE approach. This comparison is shown in Fig. 11, expressed in terms of the hyperspherical variables t and Y (in the following two paragraphs, the standard Mandelstam s and t are denoted by \tilde{s} and \tilde{t} , respectively).

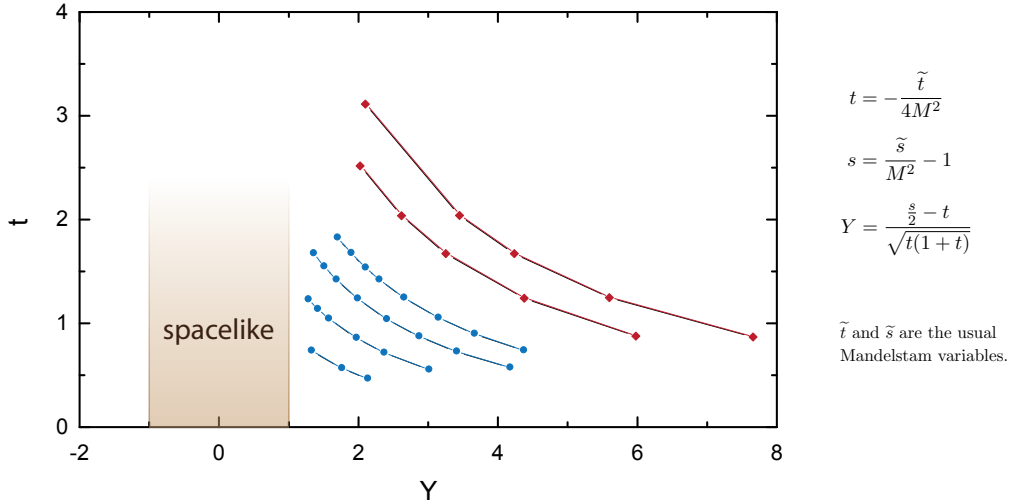


Figure 11: Existing (blue) and proposed (red) WACS data points with the phase space accessible in the DSE approach, in terms of the hyperspherical variables t and Y . The relations with the usual Mandelstam variables are included at the right margin for comparison.

At the moment the DSE approach is restricted to the space-like region, where $|Y| < 1$ and moderate values of t (i.e. $-t < 1 \dots 2$). The working assumption is that the main momentum dependence of the Compton amplitude comes from the t -channel poles at $t < 0$ and that the Y -dependence is rather moderate, so that one can make extrapolations to $Y > 1$. In order to access the time-like (or also large t) region one needs to circumvent quark singularities in the complex plane, which is work in progress [10, 27].

Ideally, one would need data close to $Y = 1$ (backward angles) at small t , which corresponds to small s , and in fact the existing E99-114 data are already well suited for a direct comparison with theory. However, even the proposed data points at large s , which are farther away from the presently calculable region, would certainly be helpful for the DSE theorists to better understand how the system behaves in this region and to constrain extrapolations. Even more specific values of t might help: the most interesting region for the DSE approach would be that of small to medium t (moderate to large Y). Namely, if it is indeed the t -channel poles that provide the dominant structure, which should be true for the handbag diagrams, then it would be helpful to know how the Compton amplitude varies as a function of Y at fixed t . Our proposed data points at small t and large Y could provide that information.

2.7 Neutral Pion Photoproduction

After Compton scattering, the next simplest wide-angle exclusive reaction is neutral pion photoproduction ($\gamma p \rightarrow \pi^0 p$). The experimental technique for the proposed experiment is well-suited to making precision cross-section measurements on this reaction, because even without detecting the second photon (from π^0 decay) the reaction $\gamma p \rightarrow \pi^0 p$ is kinematically fully determined. In addition, π^0 -photoproduction represents the dominant background process in the kinematics of WACS. (The η -photoproduction represent just a few-% contamination.)

The appropriate analysis techniques to determine both RCS and π^0 -photoproduction cross-sections have been established by the 1979 Cornell team, and have been further developed by the much more accurate E99-114 experiment in Hall A. In fact, the analysis of the differential cross-section for this channel from the E99-114 data-set is nearing completion. The extraction of the π^0 cross-section in the present experiment will be of better quality still due to the higher energy resolution of the NPS.

The extraction of the neutral-pion photoproduction cross-section does not require any modification to the experimental setup or running conditions: the π^0 data will be contained automatically in the data stream. However, the physics motivation for the measurement of the π^0 cross-section requires an extended discussion, which is not included in this proposal and is the subject of another, self-contained proposal that will be submitted independently. On the other hand, both experiments could be considered as parts of a run group.

3 Experimental Setup

The configuration of the experimental apparatus is similar to the one used in both the E99-114 (Hall A RCS [18]) and E07-002 (Hall C RCS [20]) experiments. The recoil protons will be detected in the High-Momentum Spectrometer (HMS) operating in standard configuration. The Compton-scattered photons will be detected by the Neutral Particle Spectrometer (see Figs. 12 and 13) which, along with other key equipment, is described in the following sections.

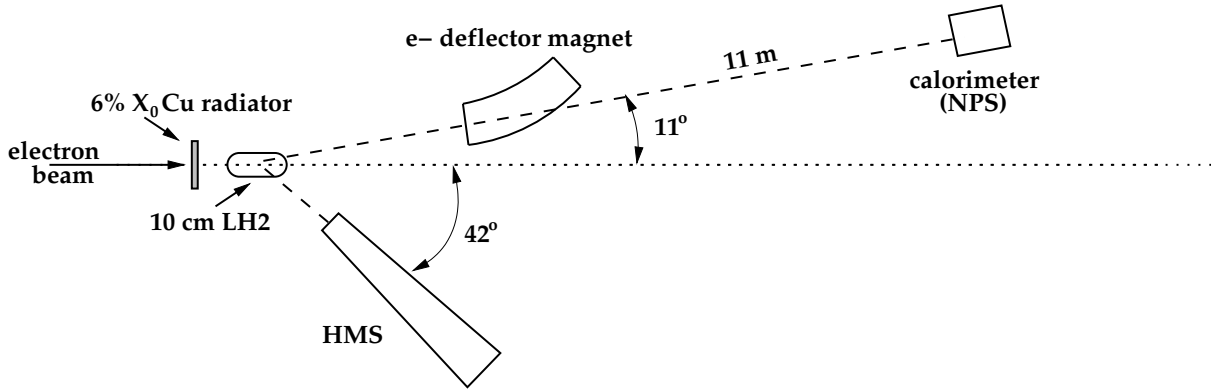


Figure 12: Schematic of the setup (kinematics 5A) at 10 GeV with the HMS detecting the recoil protons and the photon calorimeter detecting the Compton-scattered photons, in addition to a fraction of elastically scattered electrons which will be partly removed by the deflector magnet. In the real setup on the floor, the magnet will be vertically bending for reasons outlined below.



Figure 13: Proposed setup of the WACS experiment in Hall C. Looking downstream from the scattering chamber the deflection magnet, the helium bag and the calorimeter frame can be seen. The calorimeter in this configuration is located beam-left relative to the beam-pipe and on the downstream side of the SHMS spectrometer.

3.1 The CEBAF Electron Beam

Based on our experience with E99-114, we opt for an incident unpolarized electron beam with a current of up to $60 \mu\text{A}$ delivered in Hall C. Combined with the 10 cm long LH2 target, this implies a maximum luminosity of $\mathcal{L}_{\text{ep}} = 1.58 \cdot 10^{38}/\text{cm}^2\text{s}$ in the settings with the highest beam current.

3.2 The Liquid Hydrogen Target and Radiator

The experiment will utilize a standard Hall C liquid hydrogen (LH2) target with a 10 cm-long machined cell and aluminum walls of 5 mm thickness, which has been successfully employed in many experiments at JLab. A copper radiator with a thickness of $t_{\text{rad}}/X_0 = 0.06$ (6 % of radiation length) will be mounted on the cell block upstream of the cell entrance window. The distance between the radiator and target entrance window will be around 25 cm, which will allow for shielding to be installed in order to reduce scattering from the radiator onto the detectors. This distance between the target and the radiator coupled with the high incident photon energies will help to avoid background produced on the target walls and keep the photon beam spot compact. This allows both accurate measurement of the proton momentum with the vertical bend spectrometer and operation with high luminosity.

3.3 The High-Momentum Spectrometer

The recoil protons in the proposed experiment will be detected by the High-Momentum Spectrometer (HMS), which is part of the standard equipment of Hall C. The HMS is a high-resolution ($\delta p/p < 10^{-3}$) magnetic spectrometer in a QQQD configuration, with a maximum momentum of $7.3 \text{ GeV}/c$ and a momentum bite of 18 %. It has an octagonal input aperture with an effective solid angle coverage of approximately 6 msr and can be positioned at angles as low as 12.5° .

The HMS can be tuned in parallel-to-point mode (for optimal in-plane angle accuracy) or point-to-point mode (for best vertex reconstruction). In the proposed experiment it will be used in the latter mode in which extended targets can be accommodated with an *intrinsic* vertex reconstruction accuracy of $\approx 1 \text{ mm}$, and where both in-plane and out-of-plane angle resolutions are about 0.8 mrad. In the current proposal the SIMC simulation package was used for determination of the *actual* momentum and angular resolutions at each kinematic point, which included scattering in the target material and windows as well as reconstruction effects (see Sec. 4).

The detector package of the HMS consists of two drift chamber packages for track reconstruction, scintillator hodoscopes for timing, as well as a gas Čerenkov counter, an aerogel Čerenkov counter, and a segmented lead-glass shower calorimeter for particle identification. If needed, the shower calorimeter will be incorporated in the trigger for the proposed experiment in order to suppress background due to π^+ contamination.

Expected Rates

The DINREG Monte Carlo code developed by the RadCon group at JLab [35] has been used to calculate the expected proton and π^+ rates in the HMS for each of the proposed kinematic settings. The left-hand plot in Fig. 14 shows the simulated HMS singles rates, while the right-hand plot shows the simulated proton-to- π^+ ratio. The maximum HMS singles rate based upon the simulations and the proposed running conditions given in Sec. 4.3 is at point 4E and is around 50 kHz. The equivalent trigger rate (for protons only) for this same kinematic point is 7 kHz. These numbers are consistent with those observed during Hall C experiment E07-002 for which the set-up and running conditions were similar (albeit at lower beam energy). These rates are within the capabilities of the HMS [36].

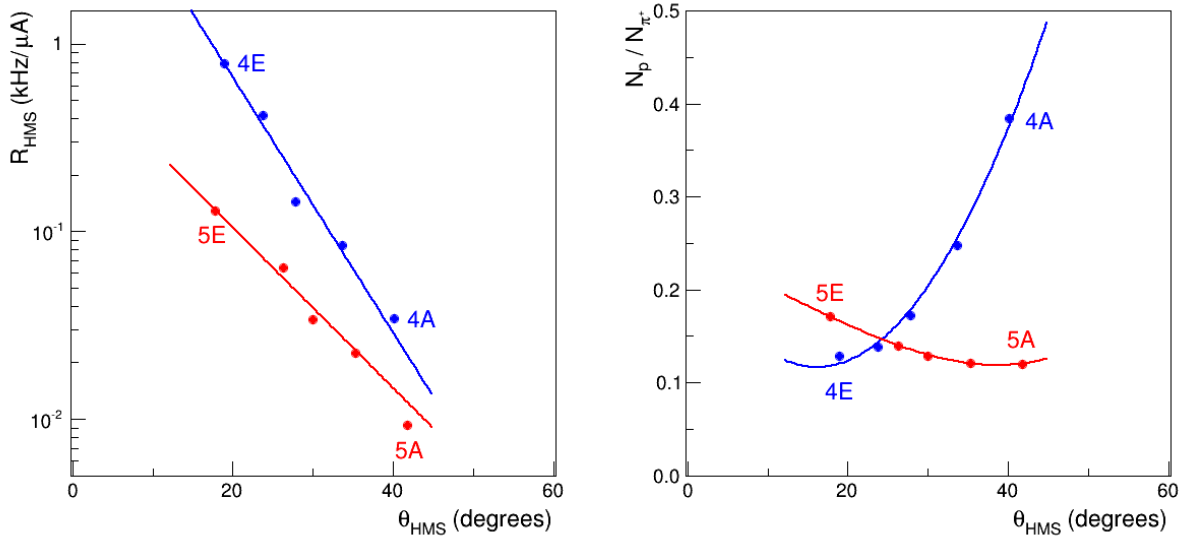


Figure 14: Simulated raw singles rates in the HMS (left) and proton-to- π^+ ratios for each of the ten proposed kinematic points. The 8 GeV data are in blue, whilst the 10 GeV data are in red.

3.4 Deflection Magnet

It was shown in the E99-114 experiment that a deflection magnet between the scattering chamber and the photon calorimeter provides an effective way to discriminate between elastic electron and photon scattering events. The magnet obviates the need for a veto detector, which in turn allows us to utilize at least ten times higher photon/electron beam intensity. The design of the magnet has been driven by a number of considerations:

- Aperture for the full size of the calorimeter;
- Value of the magnetic field for electron deflection;
- Minimum magnetic field at the beam line;
- Horizontal orientation of the magnetic field.

One of the key aspects in discrimination of Compton from background events is a reliable comparison of the expected and measured electron-proton (calorimeter-HMS) correlation. The *angular spread* of this correlation is smaller out-of-plane because it is defined only by angular resolution; in contrast, it is larger in-plane because its dominant contribution comes from the proton momentum resolution. Typically the out-of-plane resolution relevant for the e-p correlation is twice as good as the in-plane resolution. The bending direction for elastic electrons should therefore be vertical (corresponding to a horizontal magnetic field) in order to minimize the required deflection of electrons and the resulting value of the field integral required for the deflection magnet.

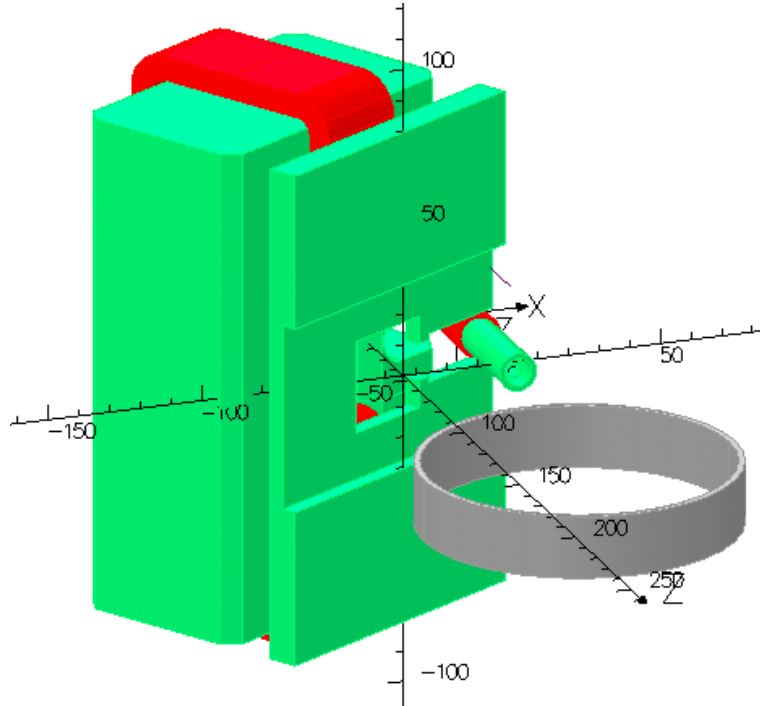


Figure 15: An image of the deflection magnet for the WACS experiment from the TOSCA analysis package, with the magnet placed at a 30 degree scattering angle with 110 cm between the magnet center and the target.

The energies of the proposed experiment are about twice as large as those encountered in E99-114, with the consequence that the angular distribution (and the corresponding spatial distribution at some drift distance) of decay photons from photo-produced π^0 events will be rather focused, resulting in a Compton peak superimposed on a relatively narrow distribution of π^0 decay photons. This means that the shape of the pion background events needs to be well understood. The role of the deflector magnet is therefore not only to separate the elastic electrons from Compton photons but also to relocate the electrons sufficiently far from the $\pi^0 \rightarrow 2\gamma$ events. This can be accomplished by a sufficiently strong deflector magnet. A magnet that will be able to provide a field integral of up to $\int \mathbf{B} \cdot d\mathbf{l} \approx 0.6 \text{ Tm}$ has been designed and will be constructed for the proposed experiment. It will be placed as indicated in Fig. 13, which shows a typical setup.

At large scattering angles, when the required solid angle of the photon arm is very large, the calorimeter will be placed very close to the target (2.5 m), which results in a significant

required 0.6 Tm field integral in the magnet. Due to the considerations above, we propose to construct a deflection magnet as shown in Fig. 15. It will have a weight of 9.5 tons and require 150 kW power. Because of the significant width of the magnet (a total of 100 cm with a 32 cm gap), a 16 cm tall cut in the left side yoke will be made for the beam line path. Such a cut allows sufficient space for magnetic shielding of the beam line. The residual transverse field integral on the beam line is of the order of 100 Gauss-meter. It will require an additional small dipole corrector to make the total field integral on the beam line vanish.

3.5 The Photon Calorimeter

The proposed experiment is made possible due to the construction of the new Neutral Particle Spectrometer [37]. This photon calorimeter, presently under construction in Hall C, will consist of a rectangular array of $1015 = 29 \text{ (hor)} \times 35 \text{ (vert)}$ PbWO_4 crystal blocks with dimensions $2.05 \times 2.05 \times 18 \text{ cm}^3$. It also includes the associated PMTs and high-voltage (HV) dividers, as well as the corresponding mechanical and electronics systems. Figure 16 shows an array of crystal blocks that will closely resemble the one that will be used in the proposed experiment, and is based on the HYCAL [38] detector.

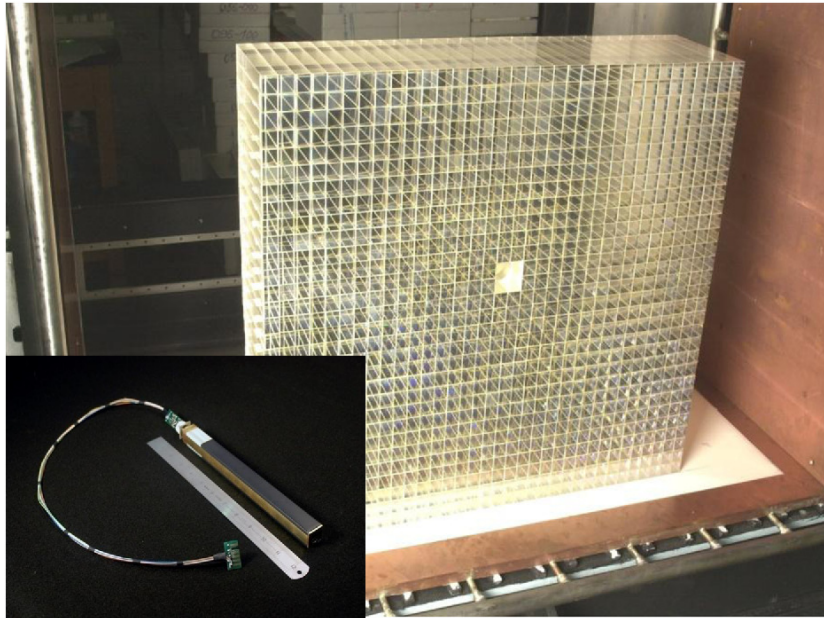


Figure 16: The high-resolution PbWO_4 part of the HYCAL detector on which the present calorimeter design is based.

The PMTs are shielded from ambient light in a light-tight box that contains an air-cooling system, whose main purpose is to prevent the PMTs from overheating and aid in the overall stable operation of the calorimeter. The yield of the PbWO_4 crystals is temperature-dependent, with around $-2\%/^{\circ}\text{C}$ deterioration of light yield around room temperature. HV and signal-cable systems are also contained in the light box encasing the PMTs.

The calorimeter will be equipped with a system that distributes light pulses to each calorimeter modules. The main purpose of this system is to provide a quick way to check

the detector operation and to calibrate the dependence of the signal amplitudes on the applied HV. The detector response to photons of a given energy may drift with time, due to drifts in the PMT gains and to changes in the glass transparency caused by radiation damage. For this reason, the gain monitoring system will also allow measurements of the relative gains of all detector channels during the experiment.

The calorimeter can be moved into the hall without being disconnected from the front-end electronics, which is located in racks a few feet behind the main detector components. The position of the photon arm will be adjusted for each kinematics to match the angular position of the HMS. The calorimeter will most likely be placed on rails and repositioned by sliding along these rails. In previous experiments less than two hours' time (beam-off to beam-on) were required to move the calorimeter in a typical hall access.

Due to radiation issues (see below) it will be very beneficial to place a 10 cm thick plastic cover with an effective surface area thickness of approximately 10 g/cm^2 in front of the calorimeter. This is motivated by experience gained during E99-114 and E07-002.

Expected Rates

DINREG Monte Carlo simulations for the expected NPS singles rates have also been performed for each of the proposed kinematic points [35]. Taking into account the proposed running conditions (given in Sec. 4.3) and the total number of γ , e^- and e^+ particles that are incident upon the calorimeter with an energy greater than 1 GeV, the maximum calculated singles rate is 1.2 MHz at the 4D setting. The variation of this rate over the proposed kinematic range is shown in Fig. 17. These simulated rates are consistent with an extrapolation based on a detailed study of the calorimeter performance during E99-114 [39].

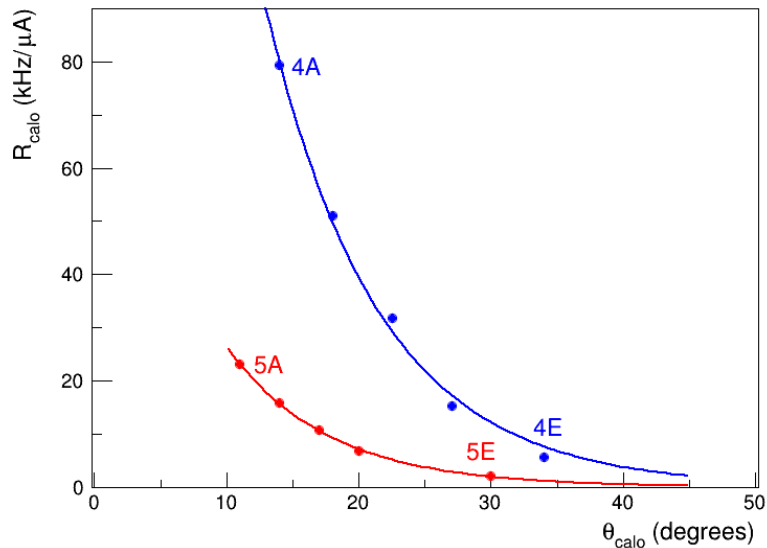


Figure 17: Simulated singles rates in the NPS assuming a 1 GeV threshold for each of the ten proposed kinematic points. The 8 GeV data are in blue, whilst the 10 GeV data are in red.

3.6 Trigger, DAQ and Computing Requirements

In contrast to E99-114, where a very particular coincidence trigger scheme was used, we *will use only the HMS trigger* in this experiment. This is possible because of the modest event rate expected in the proton arm at high photon beam energies (as described above), and because of the fact that the new HMS and NPS electronics have practically zero dead-time. This means that every proton detected by the HMS will trigger the DAQ readout of both the HMS and the NPS. The cluster summing used in the calorimeter for E99-114 and described in [39] will therefore not need to be implemented in the proposed experiment. Instead, we will take advantage of the fact that read-out of the NPS FADCs is controlled by FPGA hardware, programmed to recognise where a hit has occurred and read out only the relevant group of FADC modules, so that the generation of large amounts of non-useful data is avoided.

The PbWO_4 crystals of the NPS have a pulse length of ~ 30 ns, so that 16 samples ($16 \times 4 = 64$ ns) from the 250 MHz flash ADC will be sufficient to characterise the pulse form and base line. Monte Carlo simulations of the EM shower induced in the calorimeter suggest that the bulk of a shower will be contained in a 3×3 cluster of crystals. Online, a cluster will be signalled by a hit in a single crystal which exceeds a threshold of 25% of the elastic energy. If this and the surrounding 8 crystals are read out, a cluster will generate $9 \times 16 = 144$ data words or 288 bytes of data. It is expected that the total cluster read-out will be a factor of 2 larger than this value as a result of the inclusion of auxiliary words in the FADC readout, leading to a conservative estimate for the NPS event size of 2 kB.

Since the trigger will be formed by the HMS, the maximum data throughput will be at kinematic point 4E where, as shown in Sec. 3.3, the expected trigger rate is 7 kHz. From experience gained during E07-002, the HMS event size should be less than 2 kB. These numbers, coupled with the expected NPS singles rates given in the previous section, gives estimates for the maximum data rate in the DAQ of around 14 MB/s and for the total data-set of around 7 TB. Both these numbers are well within the capabilities of the online DAQ and data storage facilities.

3.7 Radiation Effects

The high luminosity required in the proposed experiment could result in a degradation of the energy and coordinate resolutions of the calorimeter due to pileup. Furthermore, long-term operation in a high radiation field could cause radiation damage to the crystals and loss of performance. The radiation level in Hall C during the experiment as a result of the high luminosity could also be a cause for concern. In this section, we address each of these issues using a combination of our experimental data from the E99-114 and results from our DINREG Monte Carlo simulations of the dose rates in the NPS calorimeter [35].

NPS Dose Rates

The energy of the particle detected in the calorimeter is calculated from a sum of the signals in several crystals (up to 9) which form a cluster. The noise in the ADC used for a measurement of the signal from an individual crystal contributes to the detector energy resolution. In a

high-rate experiment the ADC noise is increased, and this can be characterized by the ADC pedestal width. Using the pedestal widths observed in the E99-114 runs, the expected maximum pedestal width for the current proposal is projected to be around 50 MeV. The effect of the background on the energy resolution can then be estimated from this estimated width and the number of modules in the cluster. It is expected to be on the level of 110–150 MeV or 3.3–4.5%, with a similar estimate showing that the effect on the coordinate resolution is around 0.5 mm.

In order to estimate the potential for radiation damage to the calorimeter crystals, the DINREG simulation code has once again been used. The total dose rate incident upon the NPS calorimeter for each kinematic point and the proposed running conditions has been calculated, with the results shown in Fig. 18. The maximum expected absorbed dose rate, assuming the dose is deposited over the full crystal length, is 840 rad/h for kinematic point 4D. The corresponding total accumulated dose estimate for the full beam-time is 140 krad, although this does not include the effects of shielding the calorimeter from low energy electromagnetic radiation. Indeed, it is useful to note that interpolation of the empirical data of the E99-114 run (which included shielding) to the conditions of this proposal leads to a lower radiation estimate of 40 krad. Although these numbers are significant, they are still more than acceptable according to a study [40], which found that at a value of 1 Mrad, the light output reduction for PbWO_4 is around 2%.

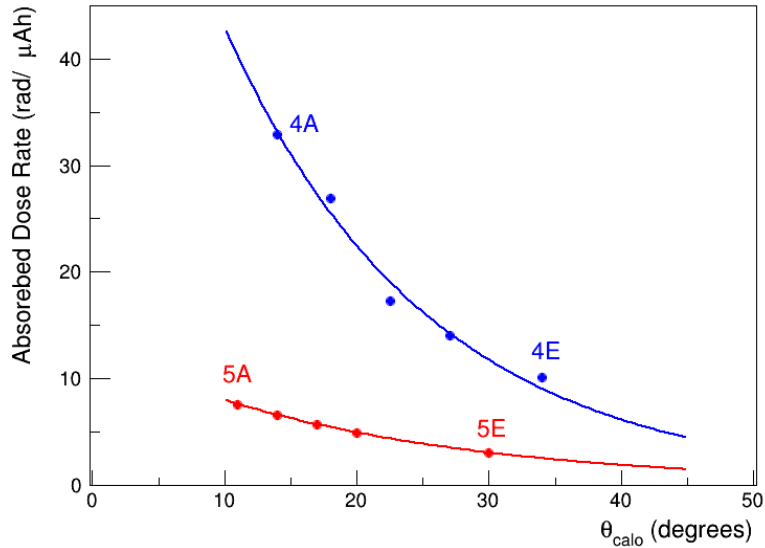


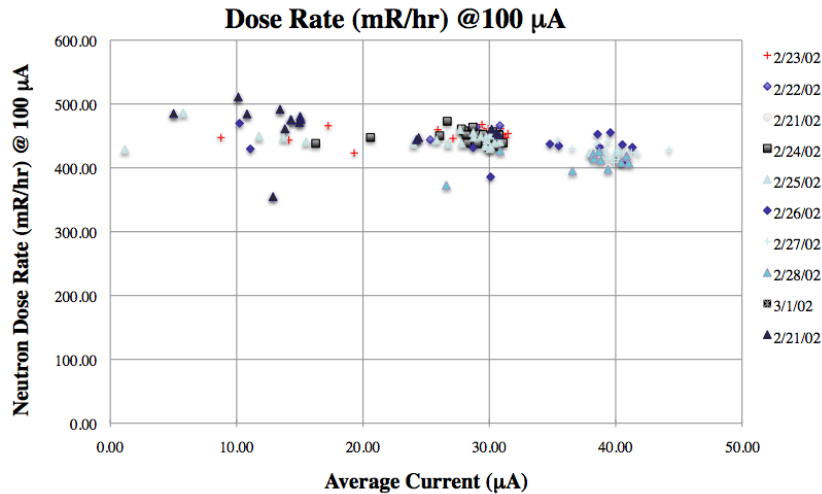
Figure 18: Simulated dose rates in the NPS as a result of all particle types at all energies for each of the ten proposed kinematic points. The 8 GeV data are in blue, whilst the 10 GeV data are in red.

Hall C Dose Rates

Using the data from the E99-114 run (Fig. 19), we also found an estimate for the radiation level in Hall C during the proposed experiment, which is of the order of 200 mrem/hour. The radiation could be reduced by a factor of 2, if necessary, by using modest local shielding of

the radiator and the target installed at angles above 50° . The maximum DINREG estimate for the dose rate in the hall for the specific proposed experiment is in agreement with the scaled-Hall A estimate.

RCS - Feb. 2002: $E_e = 3.48$ GeV



Average Dose Rate = 441. mR/hr at 100 μ A
 i.e., for a steady e^- beam of 100 μ A at $E_e=3.48$ GeV onto
 6% X0 Cu radiator followed by 15cm LH₂ target,
 the Hall A radiation monitor would record 441. mR/hr.

Figure 19: Radiation dose rate in Hall A during the E99-114 run from Ref. [41]. Note that the data applies to the beam energy of 3.48 GeV, while we will run at approximately thrice that value; but since the increase of the rate is only logarithmic in E_e , and since the data and the simulation agree at lower energies, we may safely trust the extrapolated estimates as well.

4 Proposed Measurements

The differential cross-section for wide-angle Compton scattering will be measured at photon energies of 8 and 10 GeV over a broad range of momentum transfer, allowing for determination of the dominant reaction mechanism and extraction of information on the non-perturbative structure of the proton. The following subsections give details on the proposed kinematic settings, the Monte Carlo simulation of the experimental set-up, the expected count rates for RCS and background events, and finally a discussion of systematic uncertainties.

4.1 Kinematic Settings

Kinematic variables for two standard electron beam energies of 8.8 GeV (4-pass) and 11 GeV (5-pass) over a range of scattering angles have been calculated and are summarized in Table 2. The use of a copper radiator upstream of the target produces a mixed electron-photon beam that is spread out in energy. The two-body kinematic correlation between the recoil and scattered particles means that a central point and range of incident energy is uniquely defined by the HMS angle and central momentum setting. The kinematic variables in the table correspond to a range of incident photon energies of 7.5–8.5 GeV for the 4-pass setting and 9.3–10.7 GeV for the 5-pass setting.

Table 2: Kinematics variables for WACS in five settings with a 4-pass, 8.8 GeV electron beam (4A–4E) and five settings with a 5-pass, 11 GeV electron beam (5A–5E).

Kin	E_{in} [GeV]	θ_{γ} [$^{\circ}$]	E_{γ} [GeV]	θ_{p} [$^{\circ}$]	p_{p} [GeV/ c]	θ^{cm} [$^{\circ}$]	s [GeV 2]	$-t$ [GeV 2]	$-u$ [GeV 2]
4A	8	14.2	6.347	40.1	2.416	55.8	15.89	3.10	11.03
4B	8	17.9	5.663	33.7	3.138	67.6	15.89	4.39	9.75
4C	8	22.5	4.851	27.8	3.978	80.4	15.89	5.91	8.22
4D	8	26.9	4.161	23.7	4.684	90.9	15.89	7.20	6.93
4E	8	34.0	3.255	18.9	5.605	104.8	15.89	8.90	5.23
5A	10	11.0	8.362	41.7	2.399	48.9	19.65	3.07	14.81
5B	10	13.8	7.647	35.3	3.154	59.5	19.65	4.41	13.47
5C	10	16.9	6.848	30.0	3.981	70.1	19.65	5.91	11.97
5D	10	19.7	6.158	26.3	4.687	78.7	19.65	7.21	10.68
5E	10	29.9	4.135	17.8	6.739	103.2	19.65	11.01	6.88

These kinematic settings have been chosen in order to cover a broad range of momentum transfer in the wide-angle regime, for which the Mandelstam variables s , $-t$ and $-u$ are all unequivocally larger than the typical hadronic mass scale. In all cases, the scattering angles and momenta fall well within the respective acceptances of the HMS and NPS and

pose no practical difficulties in terms of positioning of the detector systems with respect to the outgoing beam-line or other detector systems (e.g. SHMS). The incident energy range for each setting has been selected to reach as high an incident photon energy as possible and cover a reasonably narrow range in s , while also maintaining a high photon-induced event rate. Moreover, the bremsstrahlung endpoint is explicitly avoided in order to keep the electron-induced background at a manageable level.

4.2 Monte Carlo Simulation

A Monte Carlo simulation has been developed in order to study the manner in which the particles associated with the dominant physics processes will interact in the target and detector systems. Events are first generated over a much broader kinematic range than the detector acceptances according to cross-section parameterizations of the three reaction types: RCS, neutral pion photoproduction and elastic ep scattering. The parameterizations are based on extrapolation of the E99-114 data in the case of RCS and neutral pion photoproduction [16] and the Bosted fit to the Sachs form factors for elastic ep scattering events [42]. The proton interactions in the target and HMS are then simulated using the standard Hall C SIMC Monte Carlo package, while the particles scattered towards the NPS (photons, pions and electrons) are simulated using dedicated software developed within the CERN Geant4 framework. This latter package includes a realistic simulation of the target, scattering chamber, deflection magnet and NPS.

For all ten kinematic settings, this Monte Carlo simulation has been used in order to optimize the free parameters associated with the experimental set-up – i.e. the deflection magnet distance and field integral, as well as the NPS distance. This has been done in such a way as to ensure that the RCS yield extraction is as clean as possible, thereby minimizing the associated systematic uncertainties. This involves simultaneous optimization of the combined detector angular resolutions, the degree to which the scattered electrons are deflected, the relative number of background events and the RCS event rate. This process of optimization is described in more detail in the following subsections.

Data Analysis Technique

Experience gained during JLab experiments E99-114 and E07-002 has allowed for the development and refinement of a data analysis technique for identifying Compton scattered events and extracting the associated yield. The technique itself is relatively straightforward:

1. Assuming two-body kinematics, the recoil proton momentum and angle variables measured in the HMS are used to determine the energy of the incident particle that initiated the event.
2. Energy and momentum conservation then allow for the scattered photon track to be reconstructed.
3. Using the reaction vertex position from the HMS, it is then possible to predict the location of the photon hit on the calorimeter face.

4. The difference between this predicted hit position and the position of the centre of the highest energy cluster in the calorimeter (δx for in-plane and δy for out-of-plane) can then be used for event identification.
5. Figure 20 shows a typical simulated distribution of the calorimeter hit difference variables from the Monte Carlo (in this case for kinematic setting 4C). One can clearly identify three separate regions in the figure corresponding to the three primary event types:
 - RCS events are centred around $\delta_x = \delta_y = 0$ as expected from the two-body kinematic assumption made in the analysis.
 - They sit on top of a rather broad background which results from the detection of one of the photons from the decay of a photo-produced neutral pion.
 - The elastic ep events are centered at positive δy due to deflection of the scattered electron in the magnet. Although it is not obvious in this particular figure, there is also a non-negligible background contamination in the central peak as a result of elastically scattered electrons which radiate in the target or scattering chamber (so-called $ep\gamma$ events).
6. A tight central cut is placed on δ_x and then the pion background and central peak in the δ_y distribution are fitted in order to extract the total ($N_{\text{tot}} \equiv N_{\text{RCS}} + N_{ep\gamma} + N_{\pi^0}$) yield and pion ratio ($R_{\pi^0} \equiv N_{\pi^0}/N_{\text{tot}}$).
7. Finally, taking only events in this central δ_x - δ_y region and plotting their energy distribution in the calorimeter allows for the extraction of ($R_{ep\gamma} \equiv N_{ep\gamma}/N_{\text{tot}}$) and subsequently the RCS yield using the formula:

$$N_{\text{RCS}} = N_{\text{tot}} (1 - R_{\pi^0} - R_{ep\gamma}). \quad (6)$$

The major challenge in terms of robust yield extraction of the RCS signal involves separating the background events in these last two steps. It relies critically on good angular and energy resolution in the detector systems, as described in the following subsections and demonstrated in Sec. 4.4.

Detector Resolution

Two key features that have been established in previous JLab WACS experiments concerning the combined two-arm angular resolution are:

- The resolution is dominated by proton multiple scattering and reconstruction in the proton spectrometer;
- The out-of-plane (δy) resolution is much better than the in-plane (δx) resolution, as a result of the fact that the latter includes significant contributions from the proton momentum and vertex resolutions.

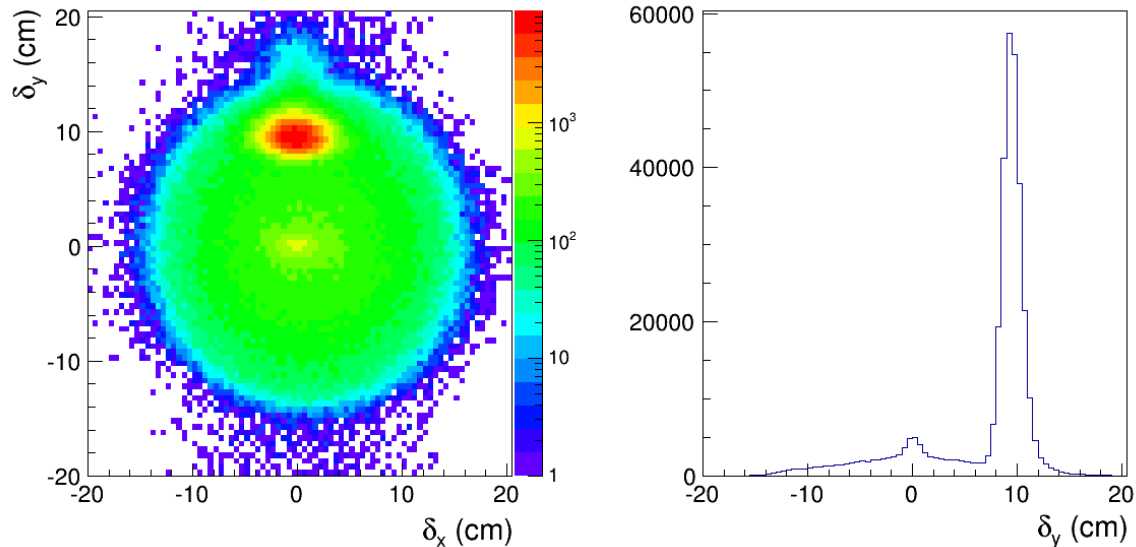


Figure 20: Typical NPS hit difference distributions for kinematic point 4C. Left: δx vs δy for all events. Right: a projection onto the δy axis for events in the central δx region.

As mentioned in Sec. 3.4, the second of these considerations, combined with the requirement for a clear separation between RCS and elastic ep events, is the reason that a horizontal magnetic field (vertical deflection) is critical to the success of the proposed experiment.

Typical values for the expected NPS position and energy resolutions have been included in the simulation, as have photon/electron interactions in the target, scattering chamber and a 10 cm plastic shield directly in front of the NPS which acts as a shield from low-energy electromagnetic background. The combination of all these contributions result in a position resolution over all kinematic settings of around 0.35 cm. For the range of proton momenta considered in the present proposal (2.4–6.7 GeV/ c), the in-plane and out-of-plane HMS angular resolutions, as well as the HMS momentum resolution, have been calculated with SIMC. The in-plane angular resolution varies between 1.5 and 2.5 mrad, the out-of-plane resolution between 1.6 and 2.7 mrad, and the $\delta p/p$ resolution between 5 and $7.5 \cdot 10^{-4}$. It is primarily the latter (although there is a small contribution from the vertex resolution) that leads to the δx resolution being poorer by as much as a factor of 4 than the δy resolution.

The distance between the target and the NPS clearly plays a crucial role in determining the final values for the combined two-arm resolution. It has therefore been optimized for all kinematic settings such that the out-of-plane resolution (σ_y) remains around or less than 1 cm. Anything larger would make extraction of the RCS signal from the pion background prohibitively difficult, leading to a large systematic uncertainty.

Physics Background

Separation of the elastic ep scattering background is achieved through the use of a deflection magnet between the scattering chamber and the NPS. In order for the separation in the out-of-plane calorimeter hit difference distribution to be sufficient for there to be no con-

tamination under the RCS peak from these background events, a deflection corresponding to greater than $5\sigma_y$ is necessary. This has been achieved by choosing appropriate values for the deflection magnet distance from the target and the field integral for each of the kinematic settings. While it would be possible for many of the proposed settings to deflect the electrons outside of the NPS acceptance, this is not desirable as a result of the need to fully understand and measure the post-scattering $ep\gamma$ events. The Monte Carlo simulation has shown that the ratio $R_{ep\gamma}$ within a region of δx - δy space centered on the RCS peak varies over all kinematic settings between 0.03 (at high $-t$) and 0.78 (at low $-t$).

Detection of one or both photons from the decay of a neutral pion leads to the dominant background in the proposed measurement. The key to extraction of the RCS signal from the pion background events on which they sit is to have as full an understanding as possible of the shape of these background events. It is then relatively straightforward to employ a mix of empirical fits and Monte Carlo simulated data to fit the pion and RCS distributions and extract the RCS yield (see Sec. 4.4). For this reason, one other critical factor in the final values chosen for the NPS distance has been to ensure that the distribution of pion events in δx and δy is not too severely artificially truncated by the NPS acceptance. The ratio R_{π^0} in the central δx - δy region as determined in the simulation varies between 0.05 (at low $-t$) and 0.90 (at high $-t$).

Optimized Photon Arm Parameters

Taking into account the considerations discussed in the previous subsections, while also trying to match the HMS and NPS acceptances in order to maintain as high an RCS event rate as possible, the simulation has been used to give the optimal values for the NPS and magnet distance and the field integral. We have also taken into account both space constraints in the experimental hall and what can be achieved with the proposed magnet design. The optimized photon arm parameters are summarized in Table 3 for the proposed kinematic settings, together with the expected σ_x and σ_y resolutions, the mean electron deflection (Δy_e) and the yield distributions for $ep\gamma$, π^0 and RCS events in the central δx - δy region.

4.3 Expected Event Rate and Statistical Precision

The expected RCS event rate for the experimental configurations given in Tables 2 and 3 has been calculated with the Monte Carlo simulation described above. The event rate is the product of the luminosity, the cross-section, and the acceptances of the detectors, as well as all other factors such as DAQ dead time, efficiency of the trigger, detectors and reconstruction analysis. The event rate \dot{N}_{RCS} has been calculated according to:

$$\dot{N}_{RCS} = \frac{d\sigma_{RCS}}{dt} \frac{(E_\gamma^f)^2}{\pi} \Delta\Omega_\gamma f_{\gamma p} \left(\frac{\Delta E_\gamma^f t_{\text{rad}}}{E_\gamma^f X_0} \right) \mathcal{L}_{\text{ep}}, \quad (7)$$

where $d\sigma_{RCS}/dt$ is the RCS cross-section; the factor $\frac{(E_\gamma^f)^2}{\pi} \Delta\Omega_\gamma$ is the range of Δt for the given kinematics, expressed through the energy of the scattered photon and the solid angle of the photon detector; $f_{\gamma p}$ is the fraction of events detected for a given range of photon energy E_γ^f ;

Table 3: Calorimeter and deflector magnet distances, deflector magnet field settings, calorimeter hit difference position resolutions, electron deflection at the calorimeter front face and estimates for the ratios $R_{ep\gamma}$, R_{π^0} and $R_{\text{RCS}} \equiv N_{\text{RCS}}/N_{\text{tot}}$.

Kin	D_{calo} [m]	D_{mag} [m]	B [T]	$\int \mathbf{B} \cdot d\mathbf{l}$ [Tm]	σ_x [cm]	σ_y [cm]	Δy_e [cm]	$R_{ep\gamma}$	R_{π^0}	R_{RCS}
4A	9.0	2.45	0.75	0.3	2.93	0.73	9.02	0.61	0.12	0.27
4B	7.0	1.65	1.00	0.4	2.21	0.75	10.74	0.37	0.33	0.30
4C	5.0	1.65	1.25	0.5	1.61	0.71	9.55	0.18	0.60	0.22
4D	3.5	1.10	1.50	0.6	1.36	0.79	9.24	0.08	0.76	0.16
4E	3.0	1.10	1.50	0.6	1.21	0.86	8.72	0.03	0.89	0.08
5A	11.0	2.45	0.625	0.25	3.42	0.70	7.53	0.78	0.05	0.17
5B	9.0	2.45	0.875	0.35	2.63	0.71	8.71	0.64	0.15	0.21
5C	7.5	1.65	1.00	0.4	2.30	0.77	9.75	0.38	0.39	0.23
5D	6.0	1.65	1.25	0.5	2.18	0.79	9.91	0.34	0.49	0.17
5E	3.25	1.10	1.50	0.6	1.26	0.92	8.07	0.03	0.90	0.07

$(\Delta E_\gamma^f/E_\gamma^f)(t_{\text{rad}}/X_0)$ is the number of photons per incident electron, including the photons produced in the target and virtual photons; and \mathcal{L}_{ep} is the electron-proton luminosity for a given beam current.

From 6, it is clear that the required number of events for each of the proposed kinematic points (N_{RCS}) depends on the statistical precision that we aim to achieve (δ_{stat}), according to the formula:

$$\delta_{\text{stat}} \equiv \frac{\delta_{N_{\text{RCS}}}}{N_{\text{RCS}}} = \frac{\sqrt{(R_{\text{RCS}}N_{\text{tot}} + R_{ep\gamma}N_{\text{tot}} + R_{\pi^0}N_{\text{tot}})}}{R_{\text{RCS}}N_{\text{tot}}}, \quad (8)$$

where the contributions to the overall statistical uncertainty as a result of fluctuations in the $ep\gamma$ and π^0 backgrounds have been included. We aim to measure the cross-sections at the kinematic points associated with the fixed $-t$ scans (4A–4D and 5A–5D) to a statistical uncertainty of 5%. However, in order to keep the beam-time request low, the high $-t$ measurements (4E and 5E) will be measured to a precision level of 8%. This sacrifice in statistical accuracy is motivated as a result of both the low cross sections and large π^0 backgrounds for these two kinematic settings. A summary of the expected event rates and required statistics is given in Table 4, together with the beam current we propose to use at each point and the required beam-time.

Table 4: RCS event rate, the total number of required events for the given statistical precision, the proposed beam current and the total beam-time for each kinematic point. The settings 4A–4E are with the 8.8 GeV beam, the settings 5A–5E are with the 11 GeV beam. The total beam-time at each point is a sum of two parts: the physics production time plus 7 hours overhead (5 hours for a LH2 run without the radiator and 2 hours for each HMS move).

Kin	θ_γ [°]	θ_p [°]	\dot{N}_{RCS} [$\mu\text{A}^{-1}\text{h}^{-1}$]	N_{RCS}	δ_{stat}	I_{beam} [μA]	t [h]
4A	14.2	40.1	15.0	1500	0.05	5	20+7
4B	17.9	33.7	6.0	1300	0.05	15	20+7
4C	22.5	27.8	3.0	1800	0.05	30	20+7
4D	26.9	23.7	1.5	2500	0.05	60	30+7
4E	34.0	18.9	0.7	2000	0.08	60	50+7
5A	11.0	41.7	9.0	2400	0.05	20	15+7
5B	13.8	35.3	3.0	1900	0.05	30	20+7
5C	16.9	30.0	1.6	1800	0.05	60	20+7
5D	19.7	26.3	1.0	2400	0.05	60	40+7
5E	29.9	17.8	0.3	2200	0.08	60	120+7
Total							425

4.4 Systematic Uncertainties

The main sources of systematic uncertainty in the proposed measurement of the WACS cross-section are summarized in Table 5. One can see that the overall uncertainty is dominated by the contributions associated with:

1. The determination of the accumulated incident photon beam flux;
2. The determination of the detector acceptances/efficiencies;
3. The extraction of the experimental Compton yield from the π^0 and $e\gamma$ backgrounds.

As before, extensive experience gained during the E99-114 and E07-002 experiments in combination with the Monte Carlo simulation studies detailed in the previous section are relied upon to make estimates of these various sources of systematic uncertainties. Beginning with the total photon beam flux, the dominant contribution is from the determination of the bremsstrahlung photon flux in a given energy range. The utilization of redundant calculations of the bremsstrahlung flux (using both Geant4 and dedicated thick-target bremsstrahlung simulation tools) and measurements using the actual data lead to confidence that this uncertainty can be kept to a minimum. The same is true in the case of the detector acceptances/efficiencies, based once again on previous experience with the HMS, the simple geometry of the NPS, and the fact that both detector systems will be operating within their respective capabilities.

Table 5: Estimated systematic uncertainties for the WACS cross-section measurement. The total is simply the individual contributions summed in quadrature.

Source	Uncertainty [%]
Incident photon flux: accumulated beam charge	1.0
Incident photon flux: target thickness	1.0
Incident photon flux: bremsstrahlung calculation	3.0
Detector: NPS detection efficiency	1.5
Detector: HMS acceptance	1.5
Detector: HMS tracking efficiency	1.5
Yield Extraction: π^0 background	3.0
Yield Extraction: $ep\gamma$ background	3.0
Total	6.0

Justification for the estimates given in the table for the extraction of the RCS yield is somewhat more involved. This estimate is subject to uncertainties from both the π^0 and $ep\gamma$ backgrounds, which vary relative to each other for different kinematic settings (as shown in Table 3). In order to estimate the magnitude of the systematic errors arising as a result of contamination from these background sources, a blind analysis of the simulated data for each kinematic point was undertaken using the analysis technique described in Sec. 4.2. As it is known that the SIMC simulation tends to somewhat underestimate the HMS resolutions [43], for the purposes of this yield extraction the resolutions have been increased by a factor of 1.5. The yield was determined from the simulated data using an empirical fit technique based on χ^2 minimization for the various distributions and then compared with the known simulated yield. PAC40 made clear that it was important to demonstrate the robust nature of this yield extraction for all kinematic settings. We have therefore included the fitted δ_y histograms for the π^0 background subtraction in Fig. 21, and the fitted E_{calo} histograms for the $ep\gamma$ background subtraction in Fig. 22. In all cases, agreement between the yield determined by blind extraction and the simulated value was around or below 3%.

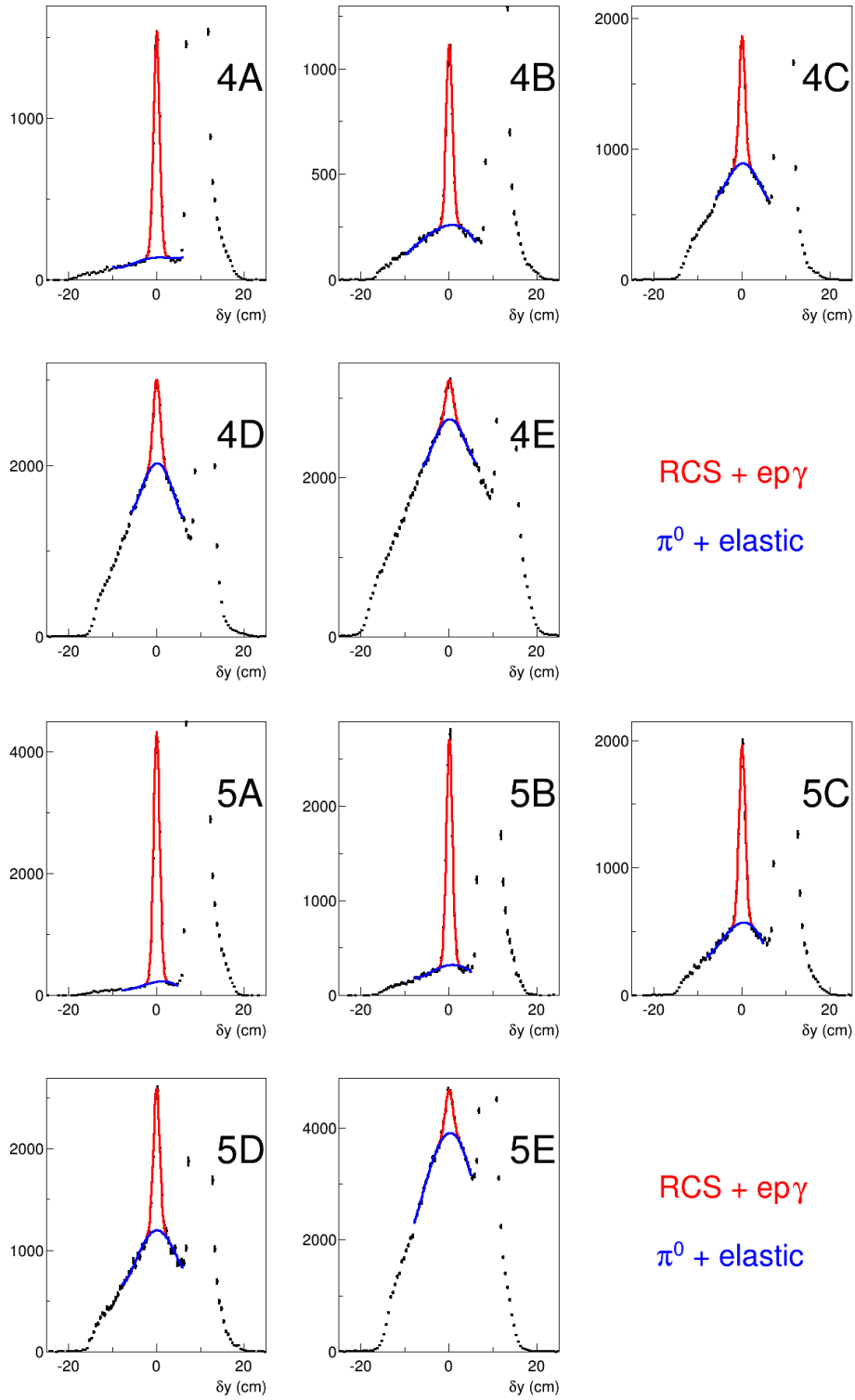


Figure 21: Empirical fits to the $RCS+ep\gamma$ (red) and π^0 +elastic (blue) event distributions in the out-of-plane hit difference (δ_y) for each kinematic point. The cuts used are $|\delta_x| < 1.5\sigma_x$ and $E_{\text{calo}} > E_{\text{RCS}}/4$. Note that the y -axis scale has been truncated to help give a clear presentation of the distributions and fits. Note that the radiative tail of the elastic peak does not contaminate the RCS signal because it extends towards the positive δ_y .

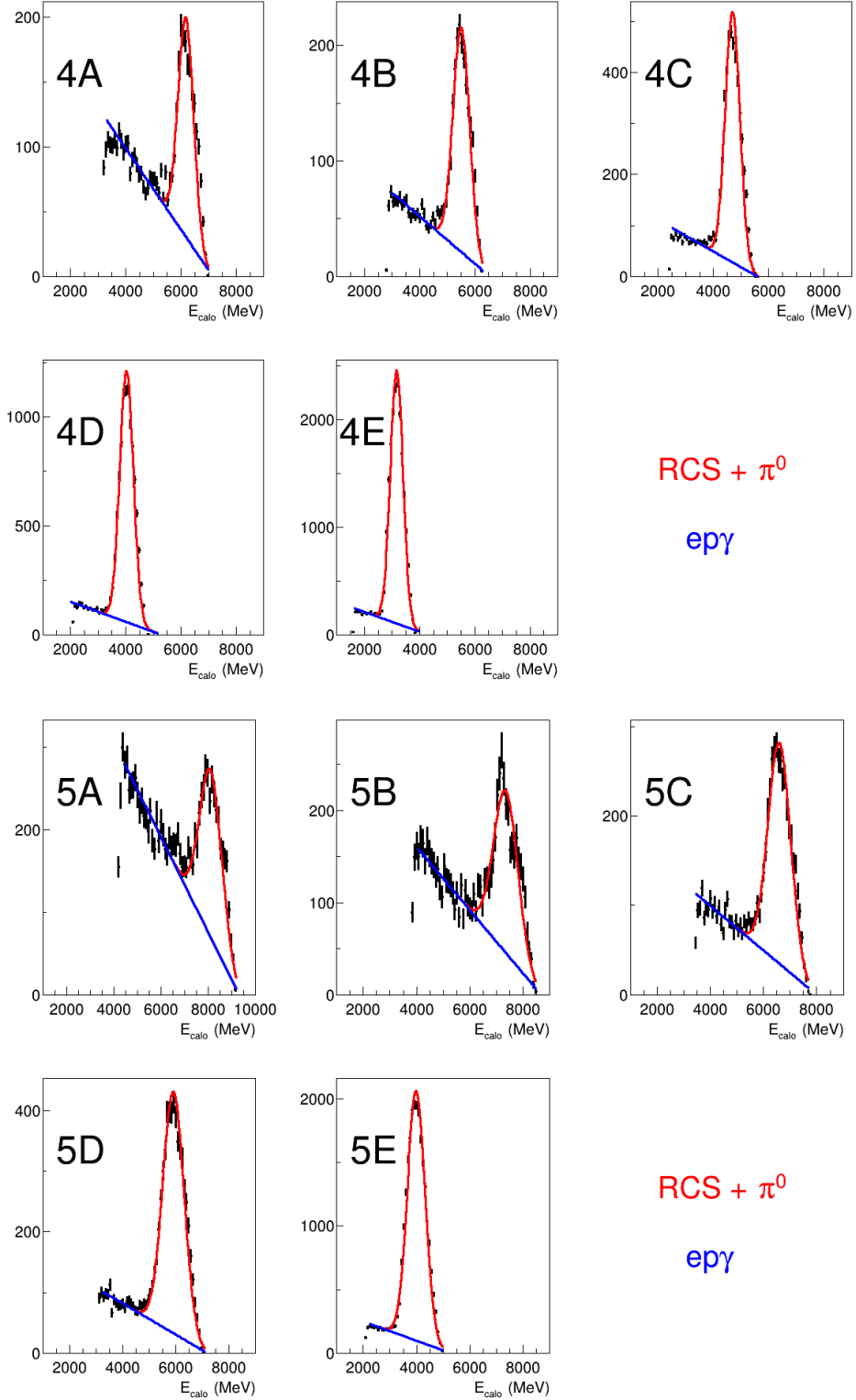


Figure 22: Empirical fits to the $RCS+\pi^0$ (red) and $e\gamma$ (blue) event distributions in the calorimeter energy spectrum (E_{calo}) for each kinematic point. The cuts used are $|\delta_x| < 1.5\sigma_x$, $|\delta_y| < 1.5\sigma_y$ and $E_{\text{calo}} > E_{\text{RCS}}/4$. Note that the blue line does not represent accurately the true distribution of the $e\gamma$ events: it is just an eye-guiding estimate.

5 Beam-Time Request and Expected Results

We propose to measure the WACS differential cross-section for photon energies of 8 and 10 GeV at eight kinematic points at moderate-to-high values of $-t$ (4A–4D and 5A–5D) to a statistical precision of 5%. We further propose measurements of two high $-t$ points (4E and 5E) at a reduced level of precision of 8% with a view to keeping the beam-time request modest. For all ten points, the expected systematic uncertainty is 6%, which means the total uncertainty (statistical and systematic) will be $\leq 10\%$. The raw beam-time numbers for production running are given in the previous section in Table 4. We anticipate that for each kinematic setting we will need additional 5 hours for accumulating data on a LH2 target without a radiator, in order to better understand the $e\gamma$ background, and 2 hours for each spectrometer move. Taken together, the resulting total beam-time request with 4-pass beam (4A–4E) is 175 hours, and 250 hours with 5-pass beam (5A–5E).

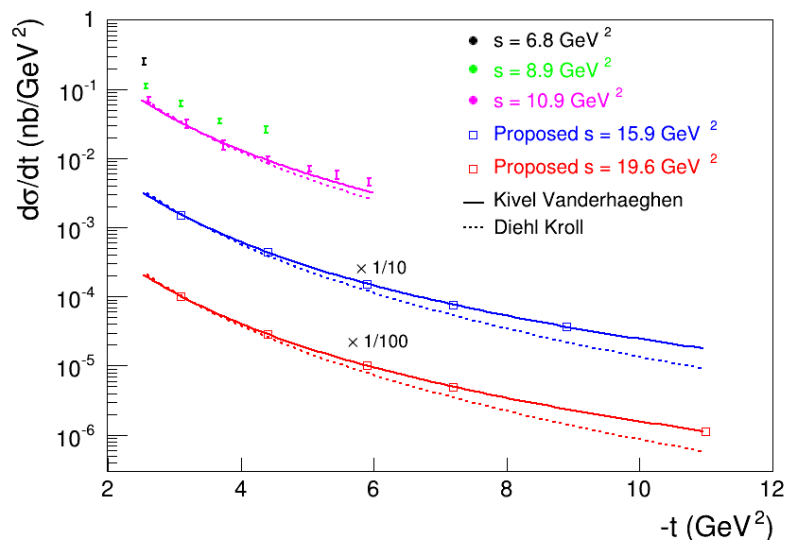


Figure 23: The anticipated data points of the proposed experiment at $s = 15.9 \text{ GeV}^2$ (open red symbols) and at $s = 19.6 \text{ GeV}^2$ (open blue symbols) for the total beam time of 425 hours, together with the existing cross-sections from E99-114 [16]. The dashed curves are the recent predictions of Diehl and Kroll (DK) [9], while the solid ones are SCET predictions from Kivel and Vanderhaeghen (KV) [7, 8]. The error bars on the expected results are combined statistical and systematic.

The current beam-time request is less than half what was proposed to PAC40, whose constructive and helpful feedback we have enthusiastically taken on board in preparing this more focused proposal. That focus is apparent when we consider the potential impact of the expected cross-section results, which are shown in Figure 23, with results from the previous Jefferson Lab E99-114 experiment also included. One obvious feature of this figure is the degree to which the proposed cross-section measurements will extend to a new and uncharted range in s and $-t$. This clearly has implications in terms of improving our understanding of the reaction mechanism and proton structure information accessible through wide-angle Compton scattering.

In order to demonstrate in detail the effect of these implications, and in light of the goals laid out in Sec 2.6, the expected cross-section results have been employed to calculate the SCET form factor \mathcal{R} introduced in Sec. 2.1. The four proposed fixed $-t$ scans for the kinematic points labelled A–D allow for a rigorous and precise exploration of the s -dependence of this form factor over an unprecedented kinematic range, as can be seen in Fig. 24. This figure clearly shows the improved understanding that will be achieved in terms of the s -behavior of \mathcal{R} , which can be directly predicted in the SCET approach. If it transpires that the promising preliminary evidence for the s -independence of this form factor is confirmed with the new results, it will represent the first direct and unequivocal evidence for factorization of the WACS reaction mechanism into soft and hard subprocesses. This will have important implications for the theoretical treatment of many other hard exclusive reactions at the intermediate energy frontier.

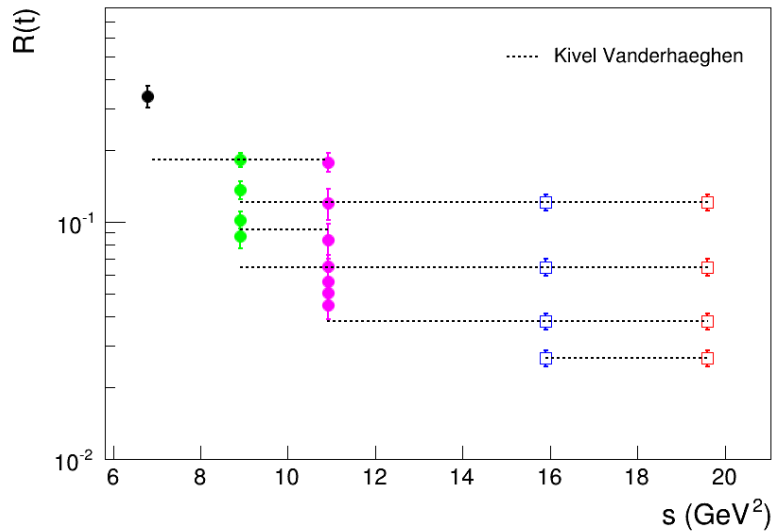


Figure 24: Extracted values for SCET form factor \mathcal{R} [7, 8] as a function of s for the previous JLab data (black, green and magenta points) and for the proposed kinematic points 4A–4D (open blue) and 5A–5D (open red). The error bars on the expected results are combined statistical and systematic.

As noted earlier, the universal nature of \mathcal{R} means that it can be used to directly constrain two-photon exchange effects in elastic electron-nucleon scattering, as well as provide valuable insights into the relationship between space-like and time-like processes. However, its evolution with momentum transfer can not be predicted from theory. It must instead be extracted from fits to experimental data, for which WACS has been identified as the most promising candidate [7, 8]. As a result, in addition to the fixed $-t$ points discussed above, the proposed measurements at $-t = 8.9 \text{ GeV}^2$ (4E) and $-t = 11.0 \text{ GeV}^2$ (5E) will almost double the $-t$ range over which the form factor can be accurately extracted. This is clearly seen in the two plots in Fig. 25, which show \mathcal{R} as a function of $-t$ and, exploring the link between WACS and elastic electron scattering, the ratio \mathcal{R}/F_1 . The improvement that can be expected in the precision achievable in the respective fits is clear.

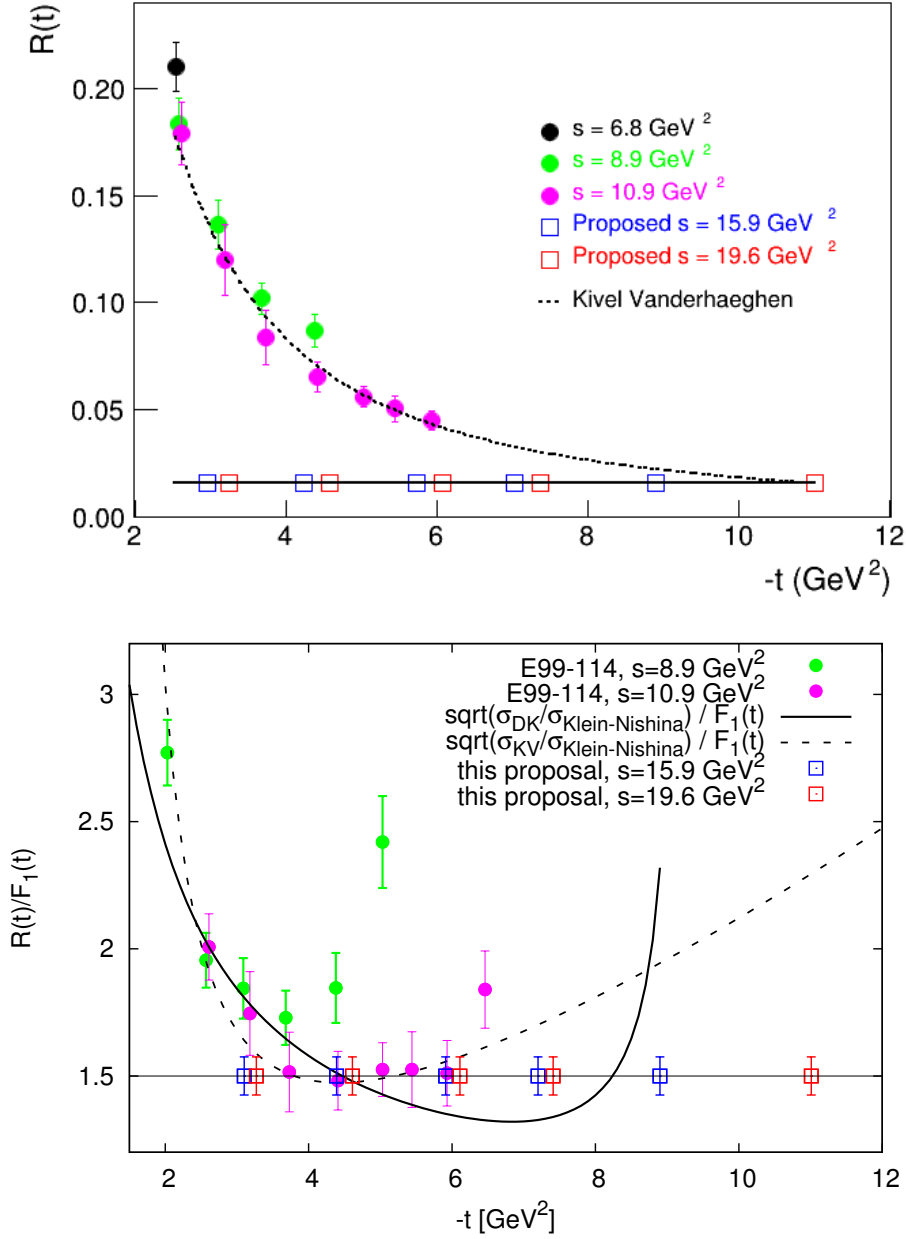


Figure 25: Expected precision of the Compton form factor \mathcal{R} (top panel) and \mathcal{R} divided by the Dirac form-factor F_1 (bottom panel) achievable with the proposed measurements (all labels as before). The curves showing the square roots of ratios of Diehl-Kroll/Klein-Nishina (DK/KN) and Kivel-Vanderhaeghen/Klein-Nishina (KV/KN) predictions correspond to $s = 10.9 \text{ GeV}^2$. In the bottom panel, the data points of the present proposal at four lowest values of $-t$ that nominally overlap in $-t$ have been slightly shifted for clarity. The error bars on the expected results are combined statistical and systematic.

6 Conclusion

We request 425 hours of beam-time (175 hours with 8.8 GeV beam energy and 250 hours with 11 GeV beam energy at beam current in the range from 5 to 60 μA) to measure the cross section for proton Compton scattering in the wide-angle regime with $\leq 10\%$ accuracy (combined statistical and systematic) at ten carefully chosen kinematic points. This experiment will take place in Hall C, utilizing the HMS spectrometer to detect recoil protons and the new Neutral Particle Spectrometer to detect scattered photons. The 10-cm long liquid hydrogen target and 6% Cu radiator will be used on the beam line. A 0.6 Tesla-meter sweep magnet will be used for the electron/photon separation. The experimental technique, as well as the analysis procedure, is tried and tested, having been successfully employed in two previous JLab experiments. The detector systems will be operating well within their capabilities, and the radiation levels incident on the calorimeter and in the hall will be manageable.

Precise knowledge of the cross section for WACS at these kinematics will allow for a rigorous test of the validity of factorization for exclusive reactions at high s and t . It will help us learn more about the interplay between soft and hard physics in determining the evolving dynamics in these types of reactions, and provide crucial insights into the fundamental nature of nucleon structure in the high- t valence region. The data will help in the understanding not just of photo-induced exclusive reactions, but in processes as diverse as the two-photon exchange mechanism in elastic ep-scattering and $p\bar{p}$ collisions.

References

- [1] A.V. Radyushkin, *Phys. Rev. D* **58**, 114008 (1998).
- [2] M. Diehl, T. Feldmann, R. Jakob, P. Kroll, *Eur. Phys. J. C* **8**, 409 (1999).
- [3] H. W. Huang, P. Kroll, T. Morii, *Eur. Phys. J. C* **23**, 301 (2002).
- [4] G. A. Miller, *Phys. Rev. C* **69**, 052201(R) (2004).
- [5] G. R. Farrar and H. Zhang, *Phys. Rev. Lett.* **41**, (1990) 1721, *Phys. Rev. D* **65** (1990) 3348.
- [6] M. Vanderhaeghen, P. A. M. Guichon and J. Van de Wiele, *Nucl. Phys. A* **622**, 144c (1997).
- [7] N. Kivel and M. Vanderhaeghen, *JHEP* 04 (2013) 029.
- [8] N. Kivel and M. Vanderhaeghen, [arXiv:1312.5456](https://arxiv.org/abs/1312.5456).
- [9] M. Diehl and P. Kroll, *Eur. Phys. J. C* **73**, 2397 (2013).
- [10] G. Eichmann and C. S. Fischer, *Phys. Rev. D* **87**, 036006 (2013).
- [11] C. D. Roberts, *Prog. Part. Nucl. Phys.* **61**, 50 (2008).
- [12] A. S. Kronfeld and B. Nizic, *Phys. Rev. D* **44**, 3445 (1991).
- [13] T. Brooks and L. Dixon, *Phys. Rev. D* **62**, 114021 (2000).
- [14] R. Thomson, A. Pang, and Cheng-Ryong Ji, *Phys. Rev. D* **73**, 054023 (2006).
- [15] F. Cano and J. M. Laget, *Phys. Rev. D* **65**, 074022 (2002).
- [16] A. Danagoulian, V. H. Mamyan *et al.*, *Phys. Rev. Lett.* **98**, 152001 (2007).
- [17] M. A. Shupe *et al.*, *Phys. Rev. D* **19**, 1921 (1979).
- [18] C. Hyde-Wright, A. Nathan, and B. Wojtsekhowski, spokespersons, JLab experiment E99-114.
- [19] D. J. Hamilton, V. H. Mamyan *et al.*, *Phys. Rev. Lett.* **94**, 242001 (2005).
- [20] R. Gilman, A. Nathan, and B. Wojtsekhowski, spokespersons, JLab experiment E07-002.
- [21] M. Diehl *et al.*, *Phys. Rev. D* **67**, 037502 (2003).
- [22] F. Cano and J. M. Laget, *Phys. Lett. B* **551**, 317 (2003).
- [23] X. Ji, *Phys. Rev. D* **55**, 7114 (1997), *Phys. Rev. Lett.* **78**, 610 (1997).

- [24] A.V. Radyushkin, *Phys. Lett.* **B 380**, 417 (1996), *Phys. Rev.* **D 56**, 5524 (1997).
- [25] C. D. Roberts and A. G. Williams, *Prog. Part. Nucl. Phys.* **33**, 477 (1994).
- [26] I. C. Cloët, C. D. Roberts, A. W. Thomas, *Phys. Rev. Lett.* **111**, 101803 (2013).
- [27] G. Eichmann and C. S. Fischer, private communication (April 2014).
- [28] G. A. Miller and M. R. Frank, *Phys. Rev.* **C 65**, 065205 (2002).
- [29] G. A. Miller, *Phys. Rev.* **C 66**, 032201 (2002).
- [30] S. J. Brodsky and G. P. Lepage in *Perturbative Quantum Chromodynamics*, edited by A. Mueller (World Scientific, Singapore, 1989).
- [31] S. J. Brodsky and G. Farrar, *Phys. Rev. Lett.* **31**, 1953 (1973).
- [32] V. Matveev *et al.*, *Nuovo Cimento Lett.* **7**, 719 (1973).
- [33] S. J. Brodsky and G. P. Lepage, *Phys. Rev.* **D 22**, 2157 (1980).
- [34] N. Kivel and M. Vanderhaeghen, private communication (April 2014).
- [35] P. Degtiarenko, private communication (January 2014).
- [36] B. Sawatzky, private communication (May 2014).
- [37] R. Ent, T. Horn, H. Mkrtchyan *et al.*, (NPS Working Group), *Neutral-Pion Spectrometer Facility in Hall C*, Proposal to Jefferson Lab PAC40.
- [38] M. Kubantsev *et al.*, *Performance of the PrimEx Electromagnetic Calorimeter*, AIP Conf. Proc. **867**, 51 (2006); A. Gasparyan, *Performance of PWO crystal Detector for a High Resolution Hybrid Electromagnetic Calorimeter at Jefferson Lab*, Proceedings of X Int. Conf. on Calorimetry in Particle Physics, Perugia, Italy, 29 March-2 April 2004, pp. 109-115.
- [39] D. J. Hamilton *et al.*, *Nucl. Instr. Meth. A* **643**, 17 (2011).
- [40] Ren-yuan Zhu, *Nucl. Instr. Meth. A* **613**, 297 (1998).
- [41] J. Boyce, private communication.
- [42] P. E. Bosted, *Phys. Rev. C* **51**, 409 (1995).
- [43] J. Arrington, private communication (June 2013).